Journal of Materials Chemistry B

ROYAL SOCIETY OF CHEMISTRY

PAPER

View Article Online
View Journal | View Issue

Cite this: J. Mater. Chem. B, 2025, 13, 4353

Insights into nano-ZrO_2 reinforced self-antibacterial Ti–3Cu composites *via* laser metal deposition: content-optimized bioactive nano-ZrO_2 integrated for wear resistance, *in vitro* antibacterial and biological properties

Ming-Chun Zhao,[a] Zhiyong Shi,[a] Xin Li,[a] Chaochun Zhao,[a] Wenze Wang,*[a] Dengfeng Yin[a] and Andrej Atrens[b]

Received 21st January 2025,
Accepted 4th March 2025

DOI: 10.1039/d5tb00143a

rsc.li/materials-b

Ti alloys are sensitive to fretting wear, which leads to early failure of their implants. Wear is a major factor in determining the long-term clinical performance. This work explored the increase of wear resistance in antibacterial Ti–Cu alloys, by incorporating biocompatible nano-ZrO_2 using laser metal deposition (LMD). The content of the reinforcing nano-ZrO_2 played a crucial role in performance. There was good densification quality for $\leq$3 wt%. The densification quality declined and there were macrocracks for $\geq$5 wt%. Both the prior β grains and the α grains initially decreased in size followed by coarsening as the ZrO_2 content increased, with the minimum at 3 wt%. The yield strength increased with increasing ZrO_2 content, and the elastic modulus increased from 5 wt%. The wear rate decreased initially and then increased with increasing ZrO_2 contents, reaching the lowest wear rate at 3 wt%. The corrosion resistance in body fluid was a minimum between 3 and 5 wt%, with less or more leading to a decrease in corrosion resistance. *In vitro* antibacterial tests and *MC3T3-E1* cell culture assays indicated that ZrO_2 contents of up to 10 wt% achieved good antibacterial effects while maintaining good biocompatibility. The comprehensive test results allowed screening and optimization of the processability and wear-related performance. 3 wt% ZrO_2 contents provided the best overall performance. The mechanisms for various content bioactive nano-ZrO_2 integrated for wear resistance, *in vitro* antibacterial and biological properties were explored. This work aimed to understand how ZrO_2 concentrations influenced the overall performance and to identify the optimal content for wear resistance and related biofunctionality.

1. Introduction

Commercially pure Ti (Cp-Ti) and Ti-6Al-4V are the most widely used metals for medical implants because of their lightweight, high strength, corrosion resistance and biocompatibility.[1] Ti-6Al-4V, in particular, is favored for bone implants such as joint replacements.[2] However, this alloy introduces biotoxic elements (Al and V) and, like other titanium alloys, suffers from a lack of antibacterial properties and insufficient wear resistance, leading to early implant failures.[3,4] Consequently, approximately 20% of joint replacements undergo costly and painful revision surgeries.[5]

Historically, much effort has been devoted to enhancing resistance to septic infections.[6–8] Previous work involved alloying Cp-Ti with 3 wt% Cu (hereafter, Ti–3Cu) using laser additive manufacturing, which yielded an alloy that demonstrated 99% bactericidal effectiveness against *E. coli* while maintaining biocompatibility.[9] However, Ti alloys are sensitive to fretting wear, and aseptic infections due to poor wear performance of titanium alloys are a much-larger more-serious cause of failure.[10–12] Obviously, even Ti–Cu alloys, although resistant to septic infections, are not resistant to the failure caused by aseptic loosening.[13,14] Therefore, it is urgent to improve the wear resistance of antibacterial Ti–Cu alloys.

Implanted materials undergo continuous stress-load cycling *in vivo*, constantly creating new surfaces.[15,16] Consequently, integration of biocompatible ceramics has been explored to develop titanium matrix composites, which offer a more uniform strength and wear resistance than external modifications like coatings.[17–20] Laser additive manufacturing is a preferred choice for the preparation of titanium matrix composites due to the superior densities and stability.[21–25] Nano-ZrO_2 with biocompatible properties was

[a] School of Materials Science and Engineering, Central South University, Changsha 410083, China. E-mail: 223112150@csu.edu.cn
[b] School of Mechanical & Mining Engineering, University of Queensland, Brisbane QLD4072, Australia

selected as the ceramic reinforcement, because of its biologically activity, such as promoting osteogenesis, better stability and biodistribution profile, and the antibacterial property of the nanoparticle morphology.[26–30] In addition, the laser process parameters can be selected so that the ZrO_2 exhibits diverse biocompatible strengthening morphologies in the titanium alloy matrix. Zhou *et al.*[31] prepared Ti-6Al-4V/ZrO_2 using the LMD method, and found grain refinement, a high concentration of Zr at the prior β grain boundaries, and strengthening that was dominated by lattice distortions due to solid solution. Li *et al.*[32] reinforced Cp-Ti with 3 wt% ZrO_2 produced by SLM to obtain particle-dispersion strengthening and better wear resistance. Ouyang *et al.*[33] prepared Ti-6Al-4V TMC reinforced with ZrO_2 particles produced by laser melt processing, and obtained particle-dispersion strengthening and analyzed the mechanism of the role of forming defects. Both solid solution strengthening and dispersion strengthening mechanisms by ZrO_2 can increase the strength of the titanium matrix. There is no need to dwell on specific forms of existence in the composite process.

Nevertheless, the impact of ZrO_2 ceramic content on bone implant alloys has been less explored, particularly the mechanisms influencing the properties of the alloys. For the discontinuously reinforced titanium composites (DRTC), the appropriate amount of ceramic is even more important than the addition strategy itself.[18,34–37] The amount of ceramic can affect the processability of the finished material and thus the reinforcement effect,[38] as well as the closely related wear resistance and other essential biological functions of the implant.[39,40] Therefore, the present work focused on the preparation of multi-component ZrO_2/Ti–3Cu, and evaluated the processibility, wear resistance and implant-related properties. The influence of nano-ZrO_2 content was investigated using different mass fractions of ZrO_2 ceramic powder in the composite powder. The mechanism of the influence of nano-ZrO_2 content on the wear resistance, and *in vitro* antibacterial and biological properties was explored. This work aimed to understand how different concentrations influenced the overall performance and to identify the optimal content for wear resistance and related biofunctionality. It can further complete the closed-loop study of the implantation properties of LMD ZrO_2/Ti–3Cu, a step forward to realize better content-tailored functional integrated materials.

2. Experimental procedure

2.1 Fabrication

The raw material powders were (i) argon-atomized Ti spherical powders with diameters of 45–105 μm (purity >99.85%, O <0.1%), (ii) pure Cu spherical powders with diameters of 15–53 μm (purity >99.7%), and (iii) ZrO_2 spherical powder with an average diameter of 50 nm (purity >99.9%), as shown in Table 1.

The appropriate fractions of the two metallic powders were blended using a vacuum ball milling mixer to obtain the Ti–3Cu. Then, 0, 0.5, 1, 3, 5, and 10 wt% of ZrO_2 powders were incorporated into the Ti–3Cu powder using the same vacuum ball milling to create the composite mixture of $x$$ZrO_2$/Ti–3Cu ($x$ = 0, 0.5, 1, 3, 5, 10 wt%), respectively, and were processed using an XL-F1000 YAG laser. Each group of composite powders was thoroughly mixed using a vacuum ball mill (30 rpm, 1 hour). The addition of nano-ZrO_2 reduced the optimal laser power density for manufacturing. Table 2 presents the optimal parameters determined through pre-experimental processes. After deposition, the samples were fabricated into three different shapes through cutting, grinding and polishing, as shown in Fig. 1.

Table 1 Detailed information of the powders

Powder	Size	Purity	Preparation method
Ti	45–105 μm	>99.85%	Argon atomization
Cu	15–53 μm	>99.7%	Argon atomization
ZrO_2	50 nm	>99.9%	Sol–gel

2.2 Processibility and microstructure characterization

Density and porosity measurements for all cubic samples were carried out using the Archimedes method. Microstructural analysis was carried out for typical samples. The surfaces (front, side, and top) of the cubic samples were ground, polished, and etched with Kroll's reagent. The microstructures were characterized using an optical microscope (OM). ImageJ software was used to measure and analyze the grain sizes of the samples. The microstructure of the front face of each sample was also examined using a scanning electron microscope (SEM), equipped with an energy dispersive X-ray (EDS) analyzer. Phase composition was determined *via* X-ray diffraction (XRD, D/max 2550, Japan), employing Cu Kα radiation at 40 kV and 30 mA, a 2θ range from 20° to 90°, at a scan rate of 5° min^{-1}.

2.3 Mechanical tests

The mechanical properties of all samples except Z0.5 (poorly structural-characterized compared to the other specimens) were assessed through a two-dimensional microhardness test, complemented by room temperature compression experiments. Prior to testing, the top and bottom surfaces of the cubic samples were ground and electrolytically polished. Microhardness evaluation used a microhardness tester equipped with a displacement stage to perform array-type Vickers hardness tests. These tests targeted an 8 mm × 8 mm area at the center of the top surface of the cubic samples. A load of 0.5 kg was applied for each test, with a dwell time of 10 seconds. The testing arrays were arranged at intervals of 0.4 mm along both the X and Y axes. Compression tests were conducted at room

Table 2 Optimal parameters for the LMD process

ZrO_2 content (wt%)	Labels	P (W)	v (mm s^{-1})	h (mm)	t (mm)	E_v (J mm^{-3})
0	Z0	460	10	1.4	0.25	131
0.5	Z0.5	450	10	1.4	0.25	129
1	Z1	440	10	1.4	0.25	126
3	Z3	460	12	1.4	0.25	110
5	Z5	460	13	1.4	0.25	97
10	Z10	460	15	1.4	0.25	84

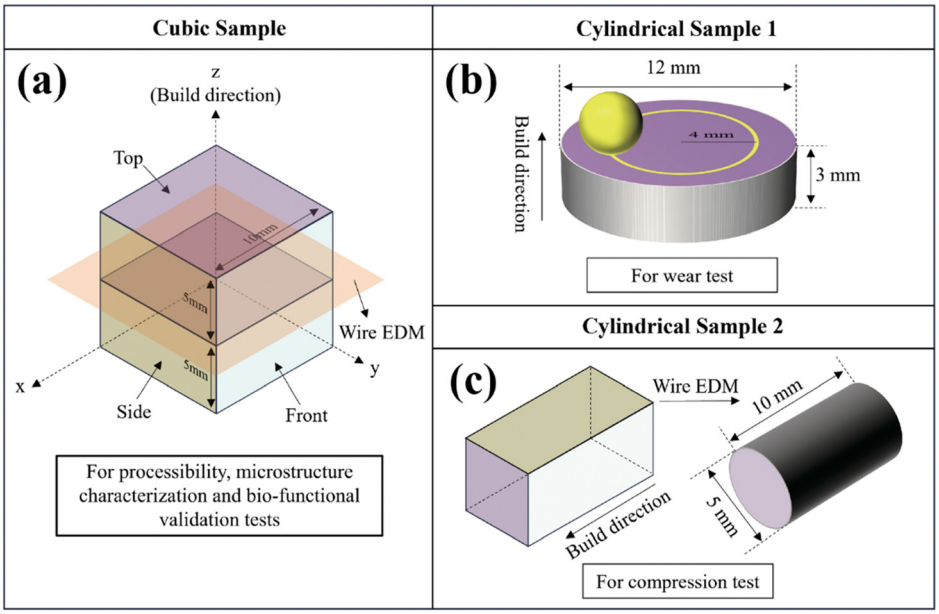

Fig. 1 Schematic of the fabricated samples: (a) cubic sample used for several tests; the cubes were produced using wire electric discharge machining (EDM); (b) the cylindrical samples used for wear test; (c) the cylindrical samples used for the compression test according to the ASTM-E9-09 standard using EDM.

temperature using a SHIMADZU AG-Xplus universal testing machine. The strain rate was 5 mm min^{-1} according to the standard ASTM E9-19.

2.4 Wear tests

Wear tests on the samples were performed in a dry friction environment, at human body temperature. These tribological assessments were conducted using a UMT-3 multifunctional friction and wear tester. The apparatus employed a ball-on-disk configuration, with a 5 mm diameter stainless steel ball serving as the friction partner. Test parameters included a load of 15N, a rotational speed of 600 rpm, and a friction ring diameter of 8 mm. Each test lasted 2500 seconds, conducted at an ambient temperature of 37 ± 1 °C. To ensure statistical reliability, each wear test was replicated three times, achieving a confidence interval of 95% within the test set. Wear rates (W) were calculated using the Archard equation:

$$W = \frac{V}{F_n l} \quad (1)$$

where V represents the wear volume, F_n the applied load, and l the wear length. Of these, the wear behavior of Z0, Z3, and Z10 was subsequently explored in further detail. The wear scars were characterized using a SENSOFAR-Sneox 3D optical profiler for 3D morphology and cross-section profile measurements. The integral of the cross-section profile was utilized to determine the wear volume. A SEM equipped with EDS was used for topographical imaging and to analyze characteristic areas of the wear scars on each test sample.

2.5 Bio-functional validation tests

2.5.1 Bio-corrosion tests. The body fluid corrosion properties of all the samples utilized a three-electrode system. The top and bottom surfaces of each sample were ground and polished. The samples were embedded so that only the top surface (10 mm × 10 mm) was exposed to the body fluid. The testing medium was Hank's solution with a pH of 7.6, composed of 8.00 g L^{-1} NaCl, 0.40 g L^{-1} KCl, 0.10 g L^{-1} $MgCl_2{\cdot}6H_2O$, 0.35 g L^{-1} $NaHCO_3$, 0.10 g L^{-1} $MgSO_4{\cdot}7H_2O$, 0.14 g L^{-1} $CaCl_2$, 0.12 g L^{-1} $Na_2HPO_4{\cdot}12H_2O$, 0.06 g L^{-1} KH_2PO_4, and 1.00 g L^{-1} glucose, maintained at a constant temperature of 37 °C.[41] Electrochemical tests were conducted using an electrochemical workstation, with a saturated calomel electrode (SCE) as the reference electrode, a platinum electrode as the counter electrode, and the test sample as the working electrode. The open circuit potential (OCP) was initially measured for 1800 seconds to ensure stability. Subsequently, Tafel curve measurements were performed within a range of −0.8 V to 0.5 V *versus* OCP. The polarization resistance (R_p) was calculated using the Stern–Geary equation:[42]

$$I_{corr} = \frac{|\beta_c| \cdot \beta_a}{2.303 \cdot R_p \cdot (|\beta_c| + \beta_a)} \quad (2)$$

where β_c and β_a are the cathodic and anodic slopes of the Tafel curve, respectively, and I_{corr} represents the corrosion current density. Electrochemical impedance spectroscopy (EIS) measurements were conducted with an acquisition frequency ranging from 0.01 Hz to 100 kHz. The EIS data were analyzed and fitted using Zsimpwin software, selecting an appropriate equivalent circuit for interpretation.

2.5.2 Antibacterial tests. *Escherichia coli* (*E. coli*, ATCC 25922) was used to evaluate the antimicrobial properties of Cp-Ti, Z3 and Z10 (together with the blank control). The square samples were autoclaved after being thinned to 2 mm thickness and placed in 24-well plates. 50 μL of cultured *E. coli* suspension (10^6 CFU mL^{-1}) was inoculated on the surface of each

sample and a polyethylene film was covered with the bacterial solution. The specimens with bacteria were incubated at 37 °C and 90% humidity for 24 h. The bacterial suspensions were rinsed, diluted and centrifuged with an appropriate amount of PBS solution. Following the Chinese national standard GB/T 4789.2, the active bacteria in the collected bacterial solution were determined by dilution plate counting, the plates were photographed at the same time, and the antibacterial rate was calculated by the proportion of colony reduction relative to the control group. In addition, the Cu release from undiluted bacterial suspensions after 24 h incubation was measured using high-frequency plasma spectroscopy (ICP-OES, SPECTRO BLUE SOP, Germany) according to the ISO standard 10993-12:2002 and ISO standard 10993-15:2000.

Fluorescence staining was used to evaluate the adhesion of the bacterial strains on different samples. After rinsing the cultured samples in Hank's solution, the samples were fixed with 4 wt% glutaraldehyde solution at 4 °C overnight. Finally, the samples were stained with a mixture of SYTO9 and PI dye (Live/Dead BacLight Bacterial Survival Kit, Invitrogen, USA) for 20 min and imaged using a laser scanning confocal microscope (CLSM, TCS SP8, Leica).

The glutaraldehyde-fixed samples were dehydrated and dried using graded ethanol solutions (20%, 40%, 60%, 80%, and 100%), were sputter plated and were imaged using SEM. These tests were conducted in triplicate and repeated three times for each group. The viability of bacteria was assessed under SEM. The criteria for determining whether bacteria are dead or alive are based on the integrity of the cell shape and the brightness differences observed in the original SEM images between the cell interior, edges, and the material matrix, as these differences help distinguish cell wall rupture and content leakage.

2.5.3 Cytocompatibility tests. *MC3T3-E1* cells (Cyagen, China) were used for biocompatibility testing of samples. Cells were cultured in 10% fetal bovine serum (Gibco) in α-minimum essential medium (α-MEM) (Hyclone). The medium was renewed every other day. 2×10^4 cells were seeded on the surface of Cp-Ti, Z3 and Z10 samples for induction of osteogenesis and cell proliferation.

During cell culture, the cell response of the samples was detected after 1 and 3 days sample culture using Cell Counting Kit-8 (CCK-8) (Beyotime, China). The cells at these two time points were soaked in paraformaldehyde at 4 °C for 4 h, dehydrated and dried with a gradient ethanol solution. The samples were sputter plated and the cells on the samples were observed by SEM. The optical density was determined at 450 nm using a microplate reader and the relative growth rate (RGR) was calculated.

The attachment and morphology of cells on different sample surfaces were observed by fluorescence microscopy. After fixing the cells with paraformaldehyde 1 and 3 days after seeding, the cells were permeabilized with 0.1% (v/v) Triton X-100 (Beyotime, China) for 5 min. Afterwards, *MC3T3-E1* cells were stained using rhodamine–phalloidin (Molecular Probes® Thermo Fisher Scientific) for 40 min to visualize the actin structure. In addition, 5 mg mL^{-1} of 40,6-diamidino-2-phenylindole (DAPI) solution was used to counterstain the cell nucleus.

3. Results

3.1 Densification

All samples attained the expected shapes under the adjusted parameters. Fig. 2(a) shows the effect of ZrO_2 content on the densification and porosity of the LMDed samples (Z0–Z10). Increasing ZrO_2 content should increase the theoretical density, since ZrO_2 has a higher density than the Ti–Cu matrix. The Archimedes method showed that the bulk density increased from Z0 to Z5, from 4.54 g cm^{-3} to 4.58 g cm^{-3}. However, even though the growth rate of ZrO_2 content increased, the increase rate of bulk density decreased. Furthermore, for 10 wt% ZrO_2, the actual density decreased to 4.523 g cm^{-3}. The porosity from Z0 to Z3 was maintained at a low level. However, the porosity rose at Z5 to 1.26%, and reached 3.5% at Z10, a relatively high value for a LMD process.

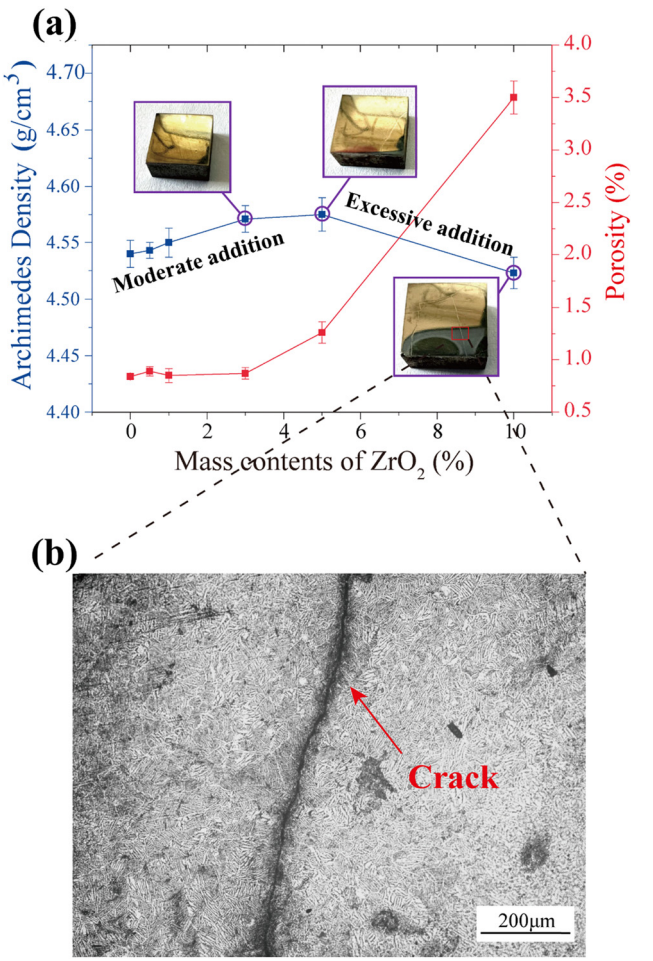

Fig. 2 (a) The porosity and Archimedes density of the as-fabricated samples with moderate/excessive ZrO_2 contents, where the sample morphologies of Z3, Z5, and Z10 are embedded as thumbnails in the graph; (b) low magnification OM images of the macro-crack from the top view of the Z10 sample.

These results indicated that there was a moderate to excessive threshold for ZrO_2 content. Excessive ZrO_2 content decreased processibility. The macroscopic sample morphology of thumbnails in Fig. 2(a) indicated that a moderate ZrO_2 (Z0–Z3) content produced samples with good completeness of the macroscopic morphology. In contrast, excess ZrO_2 (Z5–Z10) produced obvious net-like diffusion cracks on the top of the polished samples. Fig. 2(b) shows that the cracks were elongated and coherent in morphology, and the grain shape in the vicinity of the cracks was distorted. This phenomenon may be caused by an increase in residual stresses and a reduction in ductility caused by excessive ZrO_2 content.[43]

3.2 Microstructure

Fig. 3(a1)–(a3) show the optical microstructures of Z0, and Z3 and Z10 as typical, in 3D view. Low magnification side & front views exhibit obvious prior β grains, which can be morphologically classified as columnar or equiaxed. The morphology and size of each content of prior β grain are demonstrated in Table 3. Compared to the mixed morphology of Z0, with the moderate ZrO_2 content, like Z3, the prior β grains mainly consisted of finer equiaxed grains with an average size of 51 μm. But Z10 was dominated by coarser columnar grains with an average width of 99 μm and a length in millimeters.

Fig. 3(b1)–(b6) show the optical microstructures of the front side of Z0–Z10 at high magnification. All samples exhibited a lath-like martensitic structure dominated by the α/α′ phase. The martensite of Z0–Z3 was arranged in a fine basketweave pattern. The optical micrographs of Z0 (shown in b1) showed clearer grain boundaries of prior β grain. Increasing ZrO_2 content decreased the size of the α/α′ lath followed by an increase, forming a watershed between Z1 and Z3. Z3 contained coarse α/α′ grains in only a small portion of the prior β grain boundaries, resulting in the majority of basketweave grain patterns in conjunction with a few coarser near-equiaxed grains at the edges of the grain boundaries. In contrast, the grain morphologies of Z5 and Z10 were significantly coarsened overall and reached the morphology of α colonies.

SEM and the corresponding EDS images of the magnified regions of Z0, Z3 and Z10 show the morphology of grains (Fig. 4(a)–(c)) and the distribution of Cu (Fig. 4(d)–(f)) and Zr (Fig. 4(g)–(h)) in typical samples. Morphologically, the microscopic

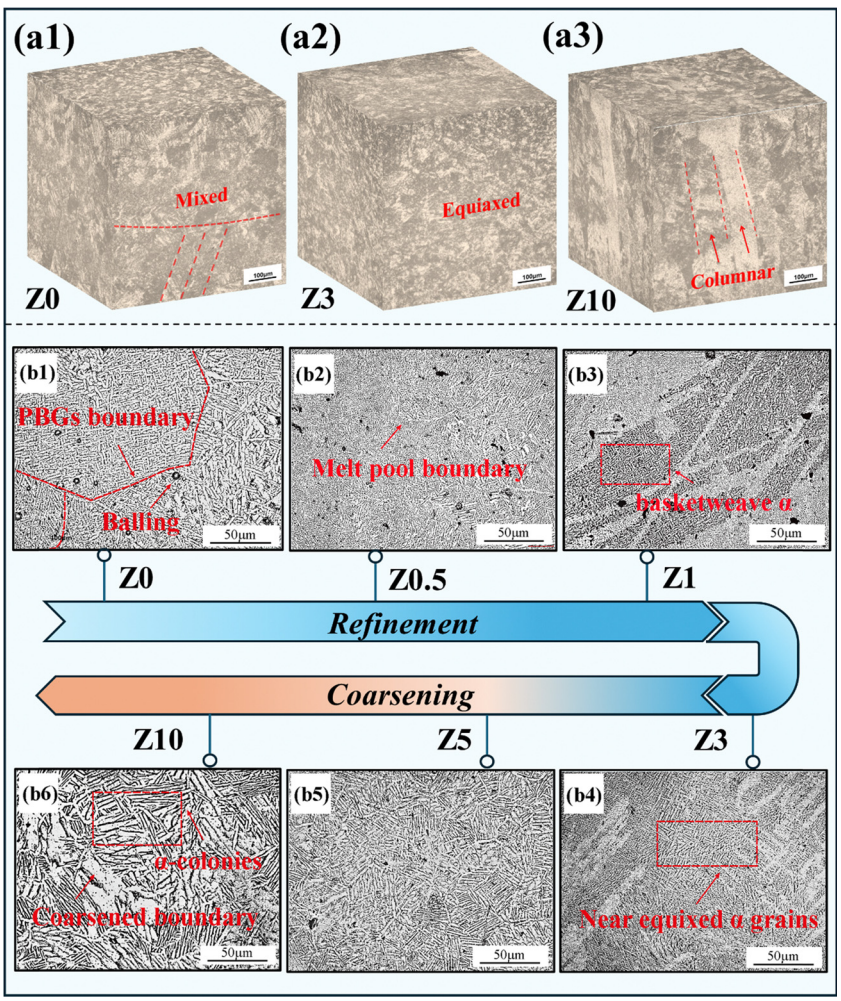

Fig. 3 Microscopic morphologies of Z0–Z10 samples: (a1)–(a3) OM 3D view of the microstructure of Z0, Z3 and Z10; (b1)–(b6) higher magnification OM images of the side views of Z0–Z10. PBG means prior β grain in b1.

Table 3 Grain morphology and size

Samples	Prior β grain morphology	Prior β grain size (μm)	α/α′ grain morphology	α/α′ grain size (μm)
Z0	Mixed	62	Basketweave	1.57
Z0.5	Equiaxed	49	Basketweave	1.12
Z1	Equiaxed	45	Basketweave	0.93
Z3	Equiaxed	51	Basketweave + equiaxed	1.36
Z5	Columnar	70	Colony	2.14
Z10	Columnar	99	Colony	3.02

defects became more obvious with increasing ZrO_2. In Z3, only tiny pores were distributed on the surface of the sample within a controllable range. In Z10, on the other hand, there were deep and wide depressions at the α grain boundaries, in which many unmelted spheres were embedded.

The distribution of Cu in Z0 was uniform, with no obvious aggregation at the micrometer scale. A ZrO_2 moderate content as in Z3 also produced a near-uniform distribution of Cu. In contrast, Cu aggregated in Z10 with a size of 2–3 μm. At this concentration, the temperatures between layers can exceed the eutectic point, resulting in a long-lasting aggregation of Cu during the continuous thermal accumulation.[44,45]

A moderate ZrO_2 content produces a uniform distribution of Zr, indicating that ZrO_2 in moderate content produces a solid-solution-based morphology, with little particle dispersion. Larger ZrO_2 contents, such as in Z10, produced a near-uniform morphology of Zr with a small amount of aggregation. The particle dispersion morphology of ZrO_2 increased in this case.

Fig. 4(i) shows the XRD patterns, which indicated the presence of the α/α′ phase. The Cu-enriched phase existed as Ti_2Cu precipitates. The characteristic peaks of the Ti_2Cu phase became more apparent with increasing ZrO_2 content, which corresponded to Cu aggregation in the EDS mapping. There were no other obvious characteristic peaks in addition to the Ti and Ti_2Cu peaks, such as ZrO_2, as the low particle content, uniform distribution and fine size of ZrO_2 were below the detection limit. EDS analysis of some characteristic points on the surfaces of Z3 and Z10 further confirmed the XRD analysis.

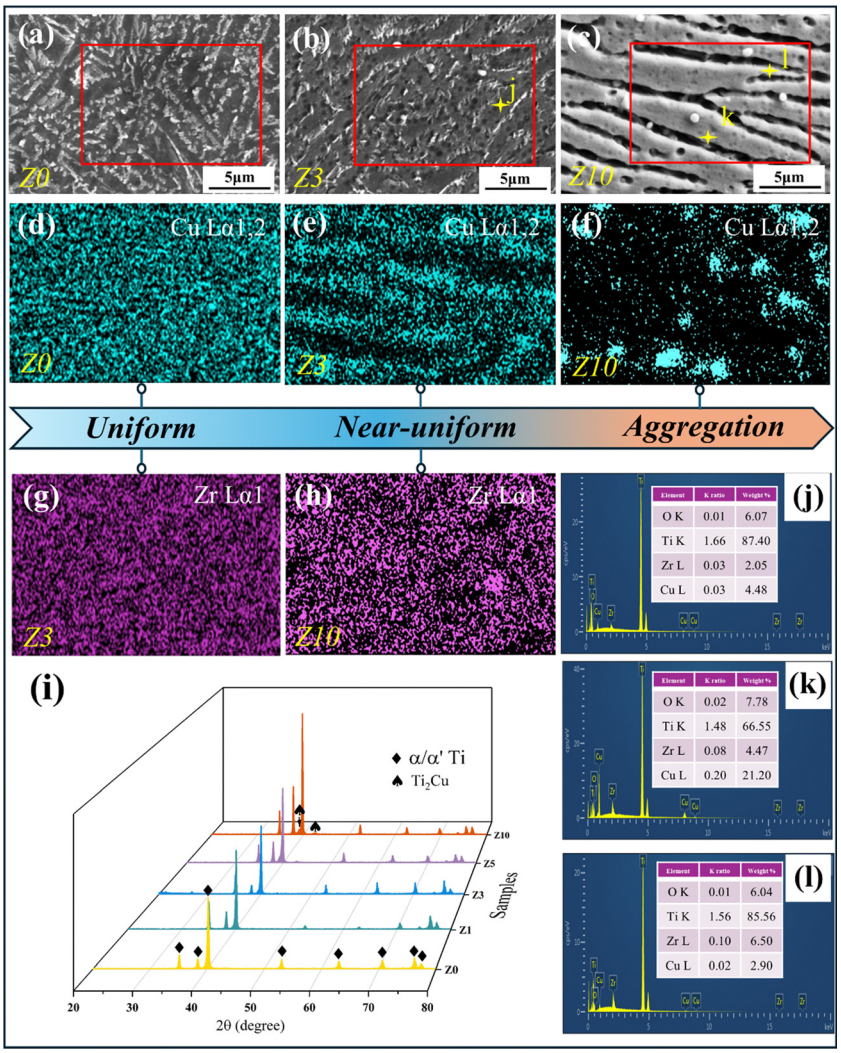

Fig. 4 SEM, EDS and XRD analysis results: (a)–(c) the SEM microstructure; (d)–(h) EDS mapping analysis of Cu (d)–(f) and Zr (g)–(h); (i) XRD pattern of the samples; (j)–(l) EDS elemental analysis results for feature points.

Point *k* in Z10 (Fig. 4(k)) had a significantly larger Cu content compared to point *j* in Z3 (Fig. 4(j)), which showed a large aggregation of Ti_2Cu. Meanwhile, point *l* of Z10 (Fig. 4(l)) had significantly increased Zr content compared to point *j* and point *k*. This indicates that there were more aggregated unmelted ZrO_2 particles in Z10.

Z3 was used as a representative to provide further insights into the microstructural characteristics. Fig. 5(a) shows the high-angle annular dark field (HAADF) image of Z3. Fig. 5(b) shows the HAADF image in higher magnification for the area marked by a white rectangle frame in Fig. 5(a). Fig. 5(c) shows the corresponding selected area electron diffraction (SAED) pattern of ZrO_2 in Fig. 5(b). Fig. 5(d1)–(d4) show the EDS map images of each element in Fig. 5(b). The second phases consisted mainly of Zr, O, and Cu. Consequently, the second phases were (Cu, Zr, O)-rich, and some ZrO_2 particles remained still undissolved. The formation mechanism of the (Cu, Zr, O)-rich second phase might be described as follows: the lower melting point Cu powders and Ti powders were melted during the LPBF-fabrication, while some of the higher melting point ZrO_2 particles that remained still undissolved acted as the nucleation site of the Cu-rich precipitates. Fig. 5(e) shows a high-resolution TEM (HR-TEM) image of the interface between the Ti matrix and ZrO_2. Fig. 5(e1) shows an inverse fast Fourier transform (IFFT) image of the interface area marked by the red rectangle frame in Fig. 5(e), which substantiated the presence of interface dislocations. Fig. 5(e2) shows an IFFT image of the Ti matrix area marked by a blue rectangle frame in Fig. 5(e), with lattice distortion, which was most likely caused by residual stress and a coefficient of thermal expansion mismatch between the ZrO_2 particles and the Ti matrix.

3.3 Mechanical properties

Fig. 6(a) and (b) show the engineering stress–strain compression curves. Table 4 summarizes the yield strength (YS), ultimate compression strength (UCS), uniform strain (ε_u), fracture strain (ε_f), Young's modulus (*E*), and Vickers hardness (HV). The increase of YS and UCS by ZrO_2 was significant. Compared to Z0, the YS of Z3 increased by 67%, while Z10 increased even more by 167%. However, the addition of ZrO_2 in excess (Z5 & Z10) caused a steep decrease in the strain at fracture due to the presence of the particles, of large quantities of residual stress and macro- or micro-cracks. In addition, although there was a significant difference in YS, the slopes of the Z0–Z3 uniform strain stage did not differ much until ZrO_2 was added in excess. This phenomenon can directly reflect the value of Young's modulus, *i.e.*, the difference of Young's modulus from Z0–Z3 was not significant, while Young's modulus of Z10 was three times greater than of that of Z3.

3.4 Wear performance

Fig. 7 summarizes the coefficient of friction (COF) and wear rate. Fig. 8–10 show the further wear test of the typical Z0, Z3, and Z10

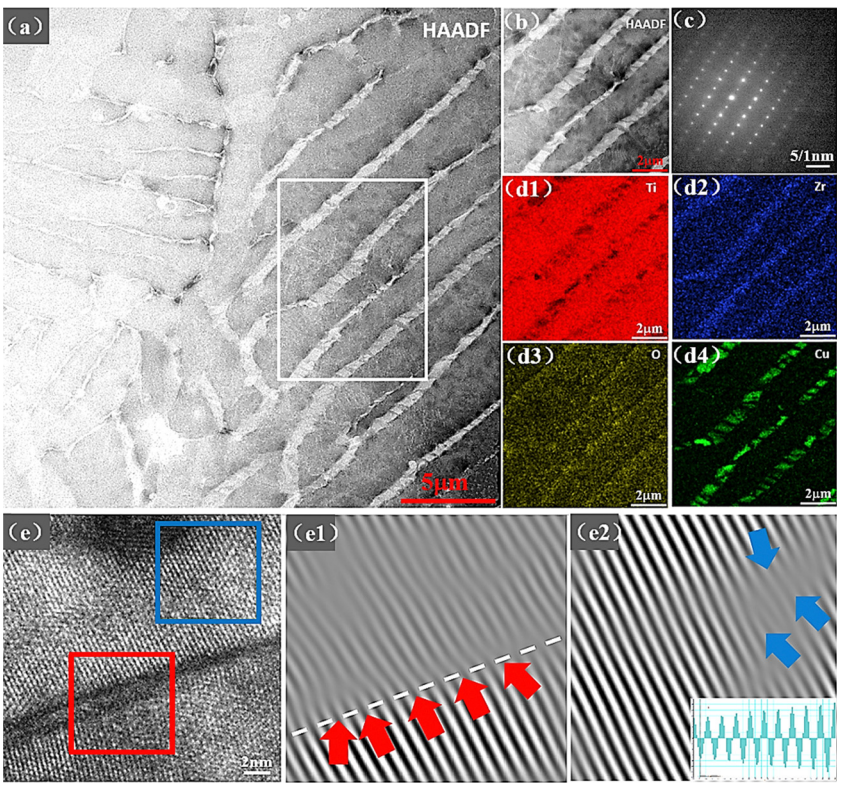

Fig. 5 (a) HAADF image of Z3, (b) HAADF image in higher magnification for the area marked by the white rectangle frame in (a) and (c) the corresponding SAED pattern of ZrO_2 in (b) and (d1)–(d4) the maps of each element in (b) and (e) HR-TEM image of the interface between the Ti matrix and ZrO_2: (e1) an IFFT image of the interface area marked by the red rectangle frame in (e), and (e2) an IFFT image of the Ti matrix area marked by the blue rectangle frame in (e).

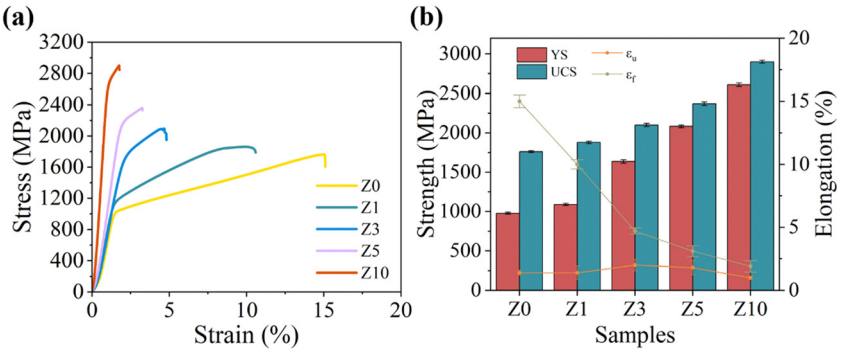

Fig. 6 (a) Engineering stress–strain compression curves; (b) summary of the mechanical property values from the room-temperature compression-test.

Table 4 Room-temperature compression properties and hardness test of the Z0–Z10 samples. (Nd means hardness in the non-defect area)

Samples	YS (MPa)	UCS (MPa)	ε_u (%)	ε_f (%)	E (GPa)	HV ($HV_{0.5}$)
Z0	979	1762	1.4	15.0	93	291
Z1	1090	1880	1.4	10.0	106	332
Z3	1637	2100	2.0	4.7	109	472
Z5	2084	2370	1.8	3.1	138	591 (Nd)
Z10	2609	2901	1.0	1.9	320	643 (Nd)

samples for detailed analysis of the characteristics and differences in wear morphology for different ZrO_2 contents.

3.4.1 Coefficient of friction. Fig. 7 shows that the COF and wear rate had a correlated trend with ZrO_2 content. Both parameters had the lowest values at the Z3 composition. The (a1) plots in Fig. 8–10 show images of the COF evolution with time for three typical samples. The average COF was 0.425 for Z0 and 0.366 for Z3 for an appropriate amount of ZrO_2, and 0.403 for Z10 for over-addition. All three samples quickly transitioned to high COF values at the beginning of the friction test. Among them, Z0 slowly increased from around 0.35 to stabilize at approximately 0.45 within the first 0–500 s. In contrast, the COF of Z3 initially rose to 0.43, then rapidly decreased and stabilized around 0.36. Meanwhile, the COF of Z10 increased to a high value of about 0.49 within 100 s, followed by a gradual decrease to around 0.4. The fluctuations of COF were largest for Z0, second largest for Z3, and were within a small range for Z10.

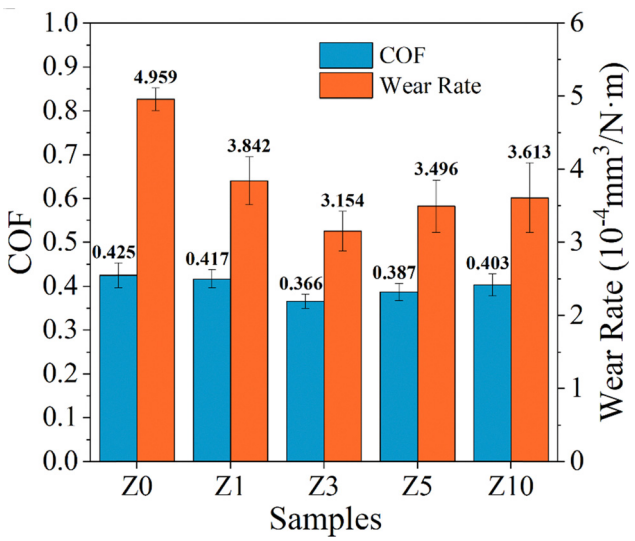

Fig. 7 COF and wear rates.

3.4.2 Wear profile. The 3D profiles are shown in (b1) of Fig. 8–10. A typical cross-sectional profile is shown in (b2). The main difference between the three samples was in the width of the wear. There was also a small difference in the depth of the wear, which was ordered according to wear volume as Z3 < Z10 < Z0. The concave wear peaks were integrated and wear rates were calculated using the wear rate equation eqn (2), as shown in Fig. 7. There was a larger difference between the wear rates of the three samples compared with the COF, with Z3 showing a 36% reduction, and Z10 showing a 27% reduction compared to Z0. The 3D profile indicated that the bottom of the wear scar of Z3 had a significantly smaller roughness than that of Z0 and Z10. The bottom roughness of Z10 was large.

3.4.3 Morphological characterization of the wear surface. Further detailed characterizations of the wear tracks at the bottom of the scar using OM and SEM are shown in (a2)–(a4) of Fig. 8–10. The wear track morphology of the Z0 sample, with no ZrO_2, was dominated by deep wide grooves along the sliding direction. These grooves were in the shape of parallel furrows that even combined with each other, indicating obvious intense plowing during sliding wear. An appropriate ZrO_2 content as in Z3 caused shallower grooves in the wear track. In addition, there were less particle debris, and fewer plate-like debris and delaminations. The significant increase in strength meant that the friction pair left less complex traces on the surface of the Z3 sample, producing a smoother wear scar. Finally, the ZrO_2 as in Z10 caused similar shallow wear, but significantly increased roughness. There were more particle debris and accumulations in large quantities around or under the delaminations. In addition, there was a small amount of micro-void on the worn surface.

3.4.4 EDS on the worn surface. Further analyses of different wear resistance mechanisms with varying ZrO_2 contents were performed using EDS analysis on the characteristic areas on the surface of the wear tracks.

The EDS analysis of the plate-like debris in Z0 (point 1), as shown in Fig. 8(c), indicated 1.8 wt% Fe from the stainless-steel

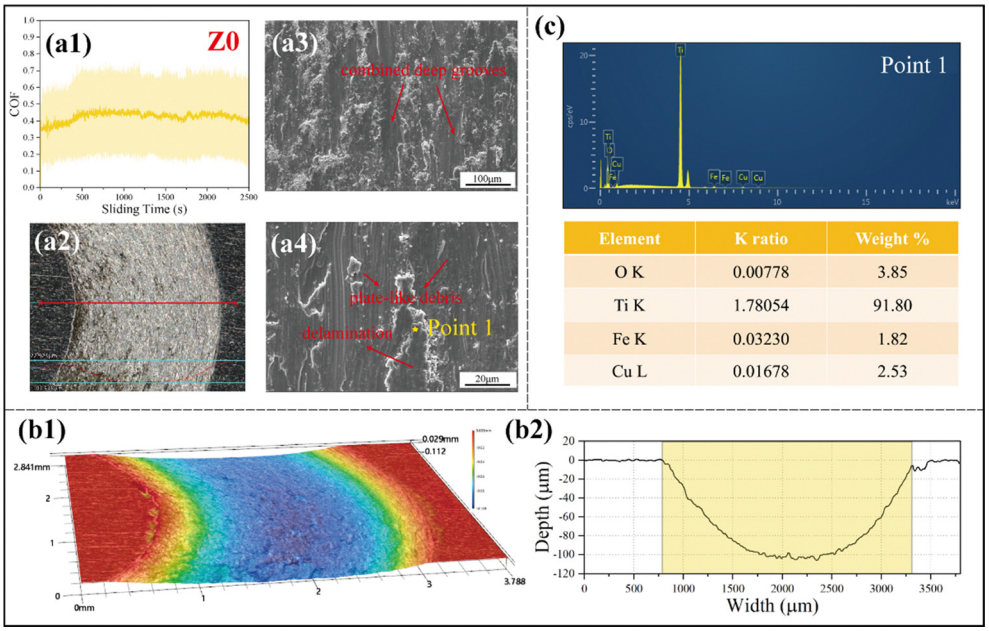

Fig. 8 Wear surface of the Z0 sample: (a1) COF curve, (a2) OM morphology, (a3) and (a4) SEM morphology, (b1) and (b2) 3D topology and corresponding 2D cross-section profiles, and (c) EDS.

ball of the friction pair, which represented few iron particles hanging from the shallow layer. This was because the abrasive particles were at a shallower position vertically and the contact with the friction pair was expected to be greater. This indicated

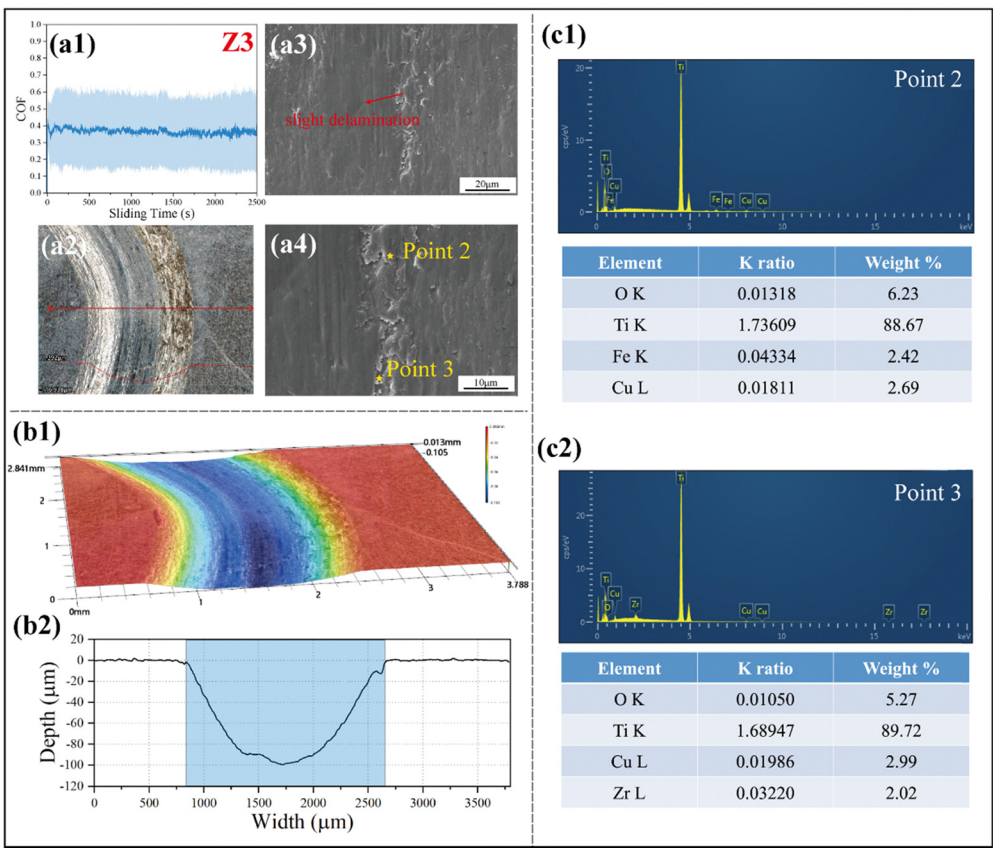

Fig. 9 Wear surface of the Z3 sample: (a1) COF curve, (a2) OM morphology, (a3) and (a4) SEM morphology, (b1) and (b2) 3D topology and corresponding 2D cross-section profiles, and (c1) and (c2) EDS.

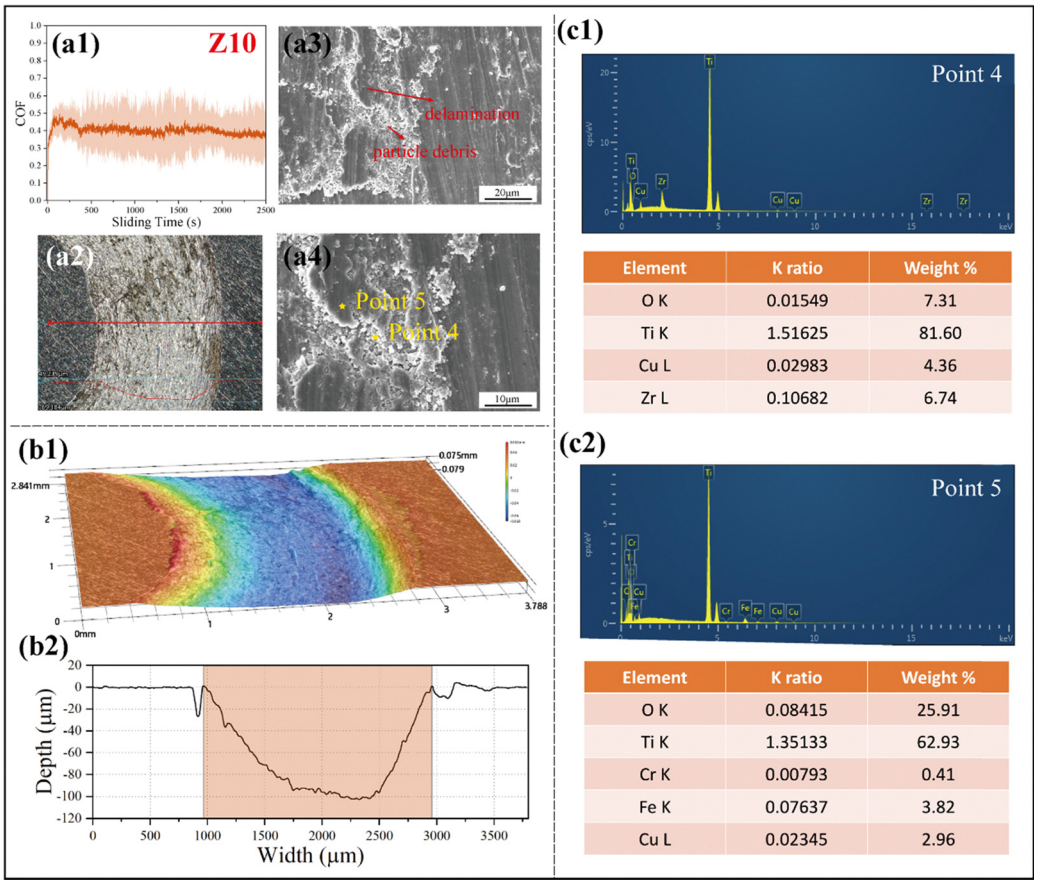

Element	K ratio	Weight %
O K	0.01549	7.31
Ti K	1.51625	81.60
Cu L	0.02983	4.36
Zr L	0.10682	6.74

Element	K ratio	Weight %
O K	0.08415	25.91
Ti K	1.35133	62.93
Cr K	0.00793	0.41
Fe K	0.07637	3.82
Cu L	0.02345	2.96

Fig. 10 Wear surface of the Z10 sample: (a1) COF curve, (a2) OM morphology, (a3) and (a4) SEM morphology, (b1) and (b2) 3D topology and corresponding 2D cross-section profiles, and (c1) and (c2) EDS.

that in addition to dominant adhesive wear, harder iron particles and matrix debris combined to cause abrasive wear.[46]

Fig. 9(a2)–(a4) shows that the width of the Z3 wear scar was significantly smaller for the appropriate ZrO_2 content. Firstly, the EDS of the surface of the delamination (point 2) (which was shallower in the vertical direction) indicated a Fe content higher for Z0 at point 1 (shown in Fig. 8(c)). This indicated that the increased strength achieved with the higher ZrO_2 content allowed for greater fallout of Fe-containing particles from the friction pair, which also caused greater abrasive wear of the Fe particles. However, the formation of fewer self-fall particles also led to a reduction in abrasive wear. EDS analysis on the interior of the delamination gap, *i.e.*, the vertically deeper point 3, indicated negligible Fe but some Zr. This indicated that friction did not remove ZrO_2 by the friction pair but these were embedded in a deeper area due to their high strength, appropriate content, fineness and roughly homogeneous distribution. The O content on the surface of the delamination was slightly larger than that in the interior, while there was Zr only in the interior that was significantly larger than that in the Z0 sample. These results indicated that the addition of ZrO_2, which has a thermal conductivity lower than that of titanium alloys, resulted in more pronounced oxidative wear in the shallowest layer.

The inner point 4 and the surface point 5 of the delamination in Z10 were analyzed by EDS as shown in Fig. 10(c1) and (c2). There was up to 26 wt% O on the surface of the delamination, but only 7 wt% of O in the interior of the delamination. Combined with the fact that there was no Zr at the surface and a greater content of Fe and Cr representing the friction pair, the addition of too much ZrO_2 greatly decreased the poor thermal conductivity of the Ti alloy matrix, which led to severe oxidative wear due to the excessive surface temperatures of the samples during cyclic wear. Spot scanning of the internal particle debris revealed a high Zr content, indicating that a large portion of this white debris was ZrO_2 particles pulled out from the matrix. The dislodged hard particles were also responsible for the microvoid on the worn surface.

3.5 Bio-corrosion in Hank's solution

Fig. 11 illustrates the Tafel curves for the Z0–Z10 samples in Hank's solution. Table 5 lists the electrochemical corrosion parameters based on the Tafel curves, using the Tafel extrapolation method as well as the Stern–Geary equation. A smaller I_{corr} with a more positive V_{corr} generally implies higher corrosion resistance. The I_{corr} increased from Z0 to Z1, decreased from Z1 to Z5, and increased from Z5 to Z10. This indicated that the corrosion resistance was ordered as Z5 > Z3 > Z0 > Z10 > Z1, which

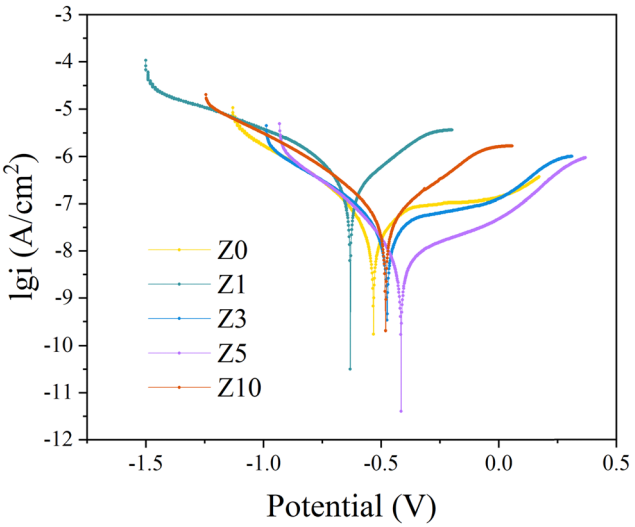

Fig. 11 Tafel curves of the samples in Hank's solution.

showed that the LMD fabrication and the addition of ZrO_2 had complex and multifaceted influences on the corrosion resistance. Compared with the R_p of Z0 (8.31×10^5 Ω), the R_p of Z3 and Z5 increased by 32% and 316%, respectively, which was satisfactory. On the other hand, Z0.5, Z1 & Z10 decreased by 85%, 91% & 64% respectively. Although their R_p values were not bad in absolute terms due to the good LMD process, the corrosion resistance was still unsatisfactory compared to that before the addition of ZrO_2.

The physiological corrosion impedance at the interface of each sample was characterized using EIS in Hank's solution. The results are shown in Fig. 12. The equivalent circuit $R(Q(R(Q(RW))))$ was used to fit the data. This circuit model uses the parameters as follows: R_s, R_f and R_{ct} refer to the solution resistance, the passivation film resistance, and the charge transfer resistance, respectively. The two CPEs refer to the constant phase elements of the alternative capacitance between the passivation film and solution, and the interface between the passivation film and material matrix. They replace the capacitance in a non-smooth plane, where the n is the exponent of CPE, which is regarded as the roughness between the interfaces. W is the Warburg impedance. The sum of R_f and R_{ct} can be considered as the polarization resistance R_p.[42] The values of each parameter fitted from the equivalent circuit are shown in Table 6.

Nyquist plots are shown in Fig. 12(a). The larger radius of the curves indicates larger corrosion resistance.[47] Fig. 12(b) shows bode plots, and in general, higher phase angles at low frequencies with larger Z modulus $|Z|$ also reflecting larger impedance with higher corrosion resistance. The Nyquist plot indicated that Z5 had the largest radius, whereas the corrosion resistance of Z1 was lower. The Bode plot showed that Z5 also exhibited a long high plateau at mid-frequency as well as a maximum $|Z|$ of 0.01 Hz, and *vice versa* for Z1. The samples all had longer frequency range plateau periods than Z0 for the phase angle plateau at mid-frequency, indicating that the appropriate amount of ZrO_2 contributed to the generation of protective films.[48] Table 6 indicated further differences between the EIS parameters. Since the passivation film resistance R_f was significantly smaller than R_{ct} due to the short test duration, the magnitude of R_{ct} was a good representation of the total polarization impedance of each sample and the degree of corrosion resistance. Compared to the R_{ct} of Z0 (8.98×10^5 Ω), the R_{ct} of Z3 was essentially the same as that of Z0, at 9.13×10^5 Ω. Z5 showed a relatively significant increase, with an R_{ct} of 3.59×10^6 Ω. Z0.5 and Z1 also exhibit low R_{ct} values, with the latter being only 2.03×10^5 Ω. The passivation film resistance R_f of Z1 had a high value of 24.71 Ω. In contrast, Z3 was only 11.92 Ω. Z5 and Z10 had passivation film resistances of 28.46 and 20.66 Ω. This seems to contradict their corrosion rates. It suggests that different ZrO_2 addition contents have complicated corrosion interfacial mechanisms, which is discussed in Section 4.4. Overall, Z3 had the same corrosion resistance as Z0, while Z5 showed better corrosion resistance, and Z10, especially Z0.5 and Z1, exhibited poorer corrosion resistance compared to Z0.

3.6 Antibacterial performance

Fig. 13(a1)–(a3) shows representative images of the bacterial colonies of the Cp-Ti sample, which was used as a control, as well as two typical contents, Z3 and Z10, after co-cultivation with *E. coli* suspensions for 24 h. The Cp-Ti had a large number of CFUs on the plate. Almost every area was covered by *E. coli* colonies. This was consistent with the fact that Cp-Ti without the antimicrobial agent Cu does not possess antimicrobial properties. Z3 and Z10 had fewer colonies on the plates than Cp-Ti, even approaching a 100% antibacterial rate.

Fig. 13(b1) shows the SEM image of *E. coli* after 24 hours of co-culturing with Cp-Ti. Most bacteria were intact and alive, marked in green, while a few were dead and marked in red. Fig. 13(b2) shows the SEM image of *E. coli* after 24 hours of co-culturing with Z3. Most bacteria were dead, marked in red, with only a few remaining alive, marked in green. A similar trend as in Ti–3Cu was shown in Z10 (Fig. 13(b3)). These results indicate that Ti–3Cu and $3ZrO_2$/Ti–3Cu have good antibacterial properties. This demonstrated excellent surface contact sterilization.[49]

Table 5 Electrochemical corrosion parameters of the samples in Hank's solution

Samples	E_{corr} (V)	I_{corr} ($\times 10^{-8}$ A cm^{-2})	$-\beta_c$ (mV per decade)	β_a (mV per decade)	R_p (MΩ)	R_p increase (*versus* Z0)(%)
Z0	−0.539	2.99	88	163	0.831	0
Z1	−0.602	53.5	198	172	0.075	−91
Z3	−0.478	1.78	75	112	1.09	+32
Z5	−0.421	0.433	51	109	3.46	+316
Z10	−0.477	10.1	138	142	0.301	−64

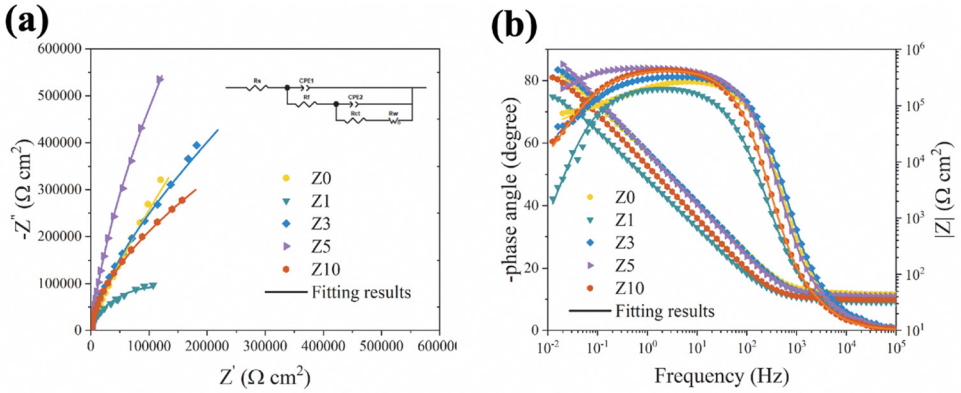

Fig. 12 Nyquist plot (a) and Bode plot (b) of the samples.

Table 6 EIS results of the samples in Hank's solution

Samples	R_s (Ω)	CPE1 × 10^6 (Ω^{-1} cm^{-2} S^{-n})	$n1$	R_f (Ω)	CPE2 × 10^6 (Ω^{-1} cm^{-2} S^{-n})	$n2$	R_{ct} (MΩ)	W (MΩ)
Z0	44.46	3.07	0.996	14.02	9.76	0.850	0.898	2.835
Z1	32.02	22.18	0.877	24.71	17.57	0.907	0.203	142.6
Z3	38.06	3.37	0.968	11.92	9.12	0.867	0.913	6.256
Z5	41.30	7.79	0.978	28.46	4.24	0.931	3.587	2.552
Z10	35.24	7.29	0.880	20.66	11.38	0.889	0.450	3.986

Fig. 13(c1)–(e4) show the results of live–dead fluorescent staining of bacteria for each of the three samples, which further examined the bacterial and biofilm adherence on the surface of the test samples. Consistent with the first two types of tests, there was a large number of surviving bacteria and a thicker biofilm on the Cp-Ti surface. In contrast, Z3 and Z10 showed a lower number of adhesions, which were essentially dead cells. In summary, Fig. 13(f) shows that the antibacterial ability of Cp-Ti was poor, with an antibacterial rate of only 2.3%. In contrast, Z3 and Z10 almost achieved a perfect antibacterial rate of 99% and 96%, respectively. In addition, Fig. 13(f) shows that the Cu ion release of Z3 was 43 μg L^{-1} and that of Z10 was 67 μg L^{-1}. This was consistent with their corrosion rates in Hank's solution. This also determined that the antimicrobial ion release of Z10 was more lethal to planktonic bacteria, which can also be echoed with the results of SEM observations.

3.7 Cytocompatibility

Fig. 14 presents the results of the osteoblast compatibility experiments for Cp-Ti and typical contents. Fig. 14(a1)–(a3) show that a higher number of live cells adhered on the surface of Cp-Ti with Z3 and Z10 in the first day of *MC3T3-E1* inoculation culture. By the third day, the cells continued to proliferate on the surface of the three samples in sizable numbers as shown in Fig. 14(a4)–(a6). Fig. 14(b1)–(b6) further demonstrate the morphology of the adherent cells by fluorescence. On one day, all surface-adhered *MC3T3-E1* showed a spindle-like morphology, with a large spreading area and tight interconnections. On the third day, almost all surfaces were covered with cells, and there was no significant difference in the density of adherent cells, which were healthy and alive. Fig. 14(c) and (d) confirmed the normal adhesion and proliferation of the cells. The absorbance on day 3 was about 6.1–7.1 times higher than that of day 1. The RGR, which symbolized the viability of the cells, were all in the normal range. These results indicated that the incorporation of 3 wt% Cu with 0–10% ZrO_2 nanoparticles did not significantly affect the good osteoblast compatibility of pure titanium.

4. Discussion

4.1 Optimization for processability

The addition of the reinforcement in the composite was not a case of "the more, the better." This study performed densification tests and microstructure characterization for composite samples with different compositions of reinforcing particles. Tests related to processability were the most direct reflection of the necessity of content screening.

There were significant differences in the thermal properties of titanium alloy matrix and ZrO_2 particles, including melting point and thermal expansion coefficient. A single small ZrO_2 particle serves as a thermal stress source due to its thermal expansion, forming micro-cracks and impeding dislocations.[33] In addition, Ti–Cu alloys have a lower melting point. As a result, most ZrO_2 particles were retained in the melt pool of Ti–Cu alloy, affecting the dynamic viscosity of the melt pool.[50] This led to a decrease in wettability and insufficient melt pool diffusion, resulting in defects. Melt pools undergo compressive stress at the surface and tensile stress at the bottom during the layer-by-layer scanning, leading to macroscopic residual stresses.[51]

At a microscopic level, the addition of excessive reinforcing particles can also negatively affect the quality of the

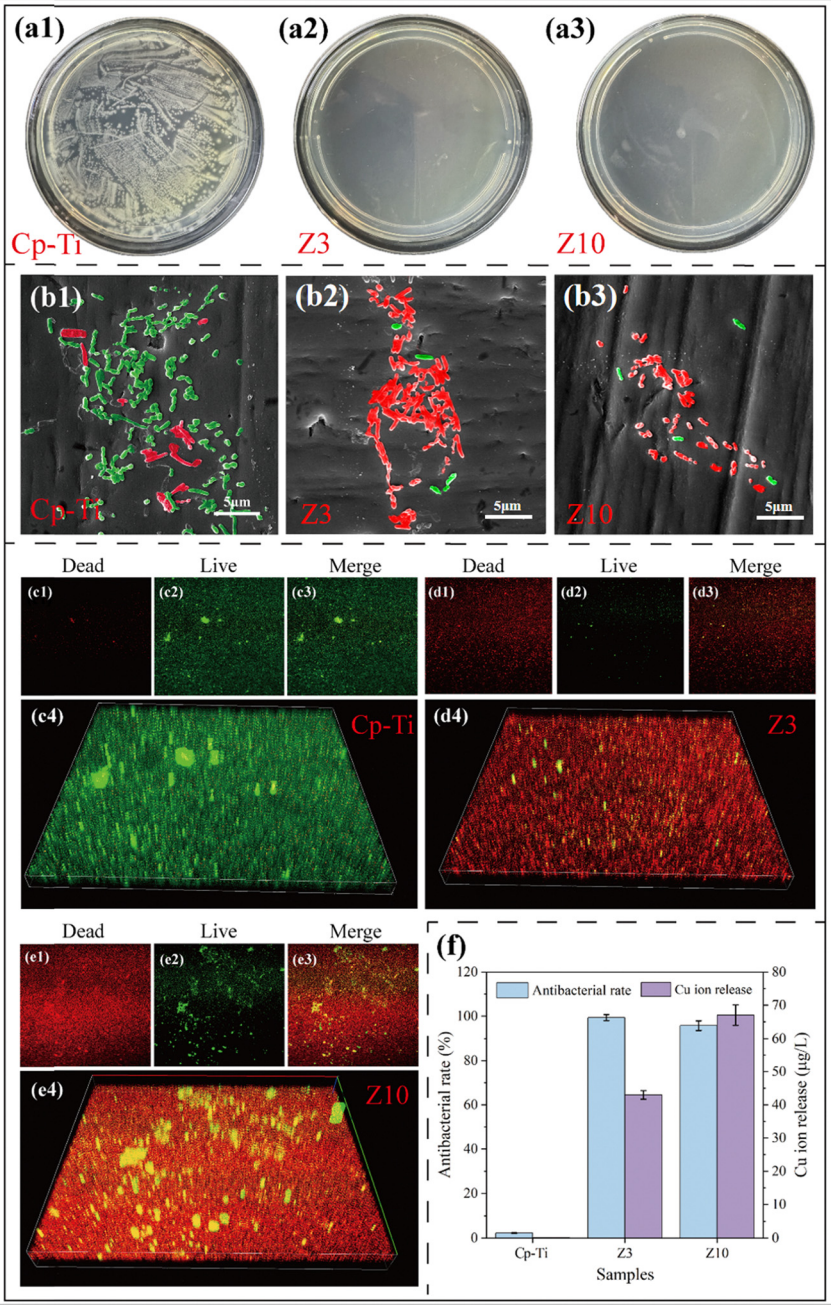

Fig. 13 *E. coli* responses to different tested samples: (a1)–(a3) typical *E. coli* colonies incubated on specimens after 24 h; (b1)–(b3) SEM observation after bacterial culturing for 24 h, with bacteria being in the stained color (dead in red and live in green). Fluorescent images of bacteria on samples of Cp-Ti (c1)–(c4), Z3 (d1)–(d4) and Z10 (e1)–(e4), alive bacteria are in green, and dead bacteria are shown in red; (f) antibacterial rate and Cu ion release.

microstructure of the sample. Moderate ZrO_2 addition can serve as heterogeneous nucleation or Zener pinning sites.[52] Solid solution of Zr has also been reported to refine the grains.[31,53] However, when added in excess, the poorer heat dissipation of ZrO_2 particles results in the growth and inhomogeneity of hierarchical grains, resulting in α colony morphology.[45]

Therefore, excessive contents of ZrO_2 (>5 wt%) proved detrimental to processability. The performance of samples with 5 wt% ZrO_2 and above exhibited a significant decrease, both macroscopically and microscopically. Consequently, ZrO_2 contents of 0–3 wt% were categorized as "moderate concentrations," while 5–10 wt% were labeled "excessive concentrations" in this study. Among these, Z3 (3 wt% ZrO_2) emerged as the optimal concentration for reinforcing particles while preserving processability. The processability, in turn, profoundly impacted the properties critical to implantable materials, as discussed in the following sections.

4.2 Optimization for wear-related performance

In real implant environments, the factors influencing the wear performance of implants can be categorized into two primary

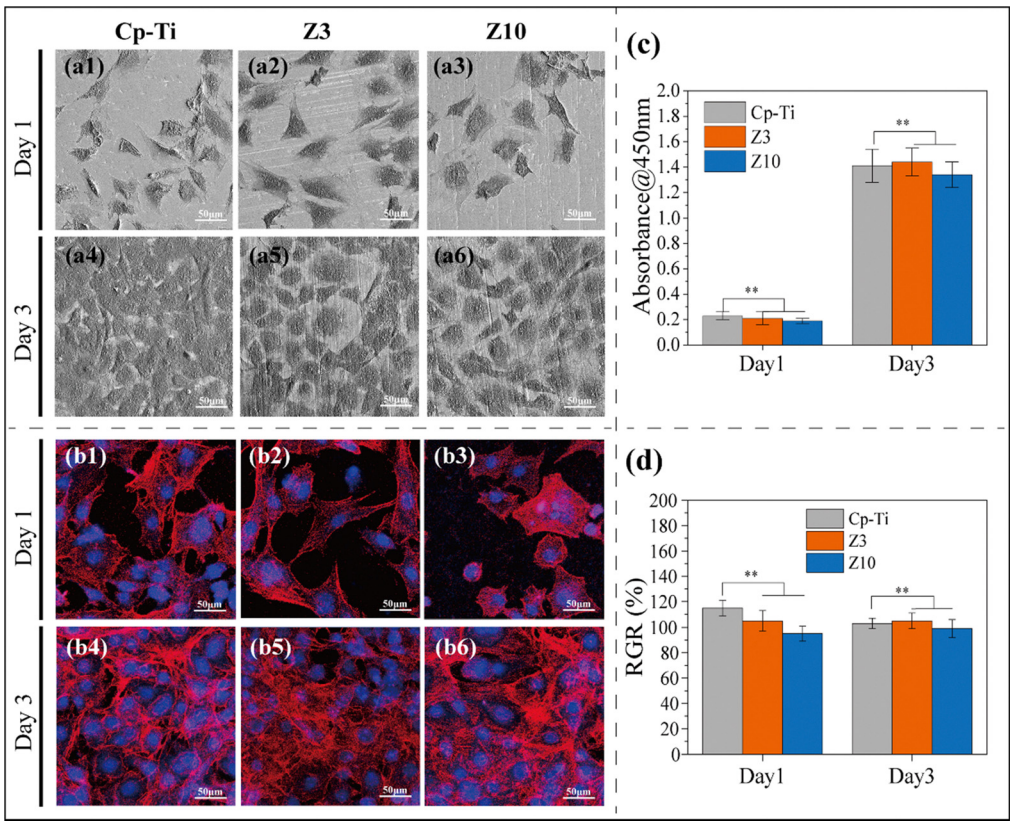

Fig. 14 Responses of *MC3T3-E1* cells to different samples: cell morphologies by SEM after culturing for 1 day (a1)–(a3) and 3 days (a4)–(a6); actin (red) and cell nucleus (blue) fluorescence staining of *MC3T3-E1* cells after culturing for 1 day (b1)–(b3) amd 3 days (b4)–(b6); proliferation (c) and cell viability (d) of *MC3T3-E1* cells cultured on different samples' surfaces for 1 day and 3 days (**$p < 0.01$, $n = 3$).

areas: mechanical-oriented factors and body fluid corrosion-oriented factors.[54] This subsection analyzes the effects of different ZrO_2 contents separately, considering the results from both categories and their correlation with wear performance.

4.2.1 Mechanical-oriented wear mechanism. The mechanical properties of the material can be almost decisive for wear resistance. In other words, the strengthening mechanism determines the mechanical behavior of the material, and the mechanical behavior determines the basic (*i.e.*, dry) wear resistance properties. Dong *et al.*[55] indicated that the pure wear loss of titanium alloys in corrosive media can account for about 85% of the total mass loss.

The microstructural and mechanical tests indicated that there were different strengthening mechanisms in composites with varying ZrO_2 contents. For moderate ZrO_2 contents, the formation of ultrafine prior β grains and α/α′ grains are the key features. However, the differences in grain size among different ZrO_2 contents were minimal, indicating a small contribution from grain refinement strengthening. Instead, solid solution strengthening and Orowan strengthening were the predominant mechanisms contributing to the overall strength in this study. With increasing ZrO_2 content, the presence of unmelted ZrO_2 particles in the melt pool became more pronounced, enhancing the strength contribution from Orowan strengthening. These hard ZrO_2 particles impede dislocation motion, thereby increasing strength, and increasing the elastic modulus. This effect was evident from the compressive mechanical property curves, which showed an increase in the elastic modulus starting from Z5, indicating a substantial accumulation of unmelted ZrO_2 particles. Additionally, when ZrO_2 is added in excess, the mismatch between the thermal expansion coefficients of ZrO_2 and the matrix led to dislocation buildup and residual stresses, further impacting the mechanical properties. The different emphasis on the strengthening mechanisms also contributed to the different dry wear performance. Fig. 15 summarizes the wear characteristics of different ZrO_2 contents and their correspondence in a real implantation environment.

When there was no ZrO_2 or the concentration was small, the lack of strength caused the tangential shear force of the bone friction pair to substantially exceed the plastic yield limit of Z0. Consequently, plowing became the primary cause of material loss. The volume loss due to adhesive wear, denoted as $\omega_{adhesive}$, was the main component of pure wear loss for Z0 and can be modeled by the following equation[56]:

$$\omega_{adhesive} = K_{trans}\int_0^t \mathrm{COF}(t)\cdot\frac{F_n\cdot v}{H(t)}\mathrm{d}t \quad (3)$$

where $\mathrm{COF}(t)$ is the COF of the wear at moment t, v is the linear velocity of the wear, $H(t)$ is the instantaneous hardness at moment t, and K_{trans} is a constant for unit conversion associated with the wear regime. For Z0, the homogeneous microstructure made $H(t)$ homogeneous but small, which together

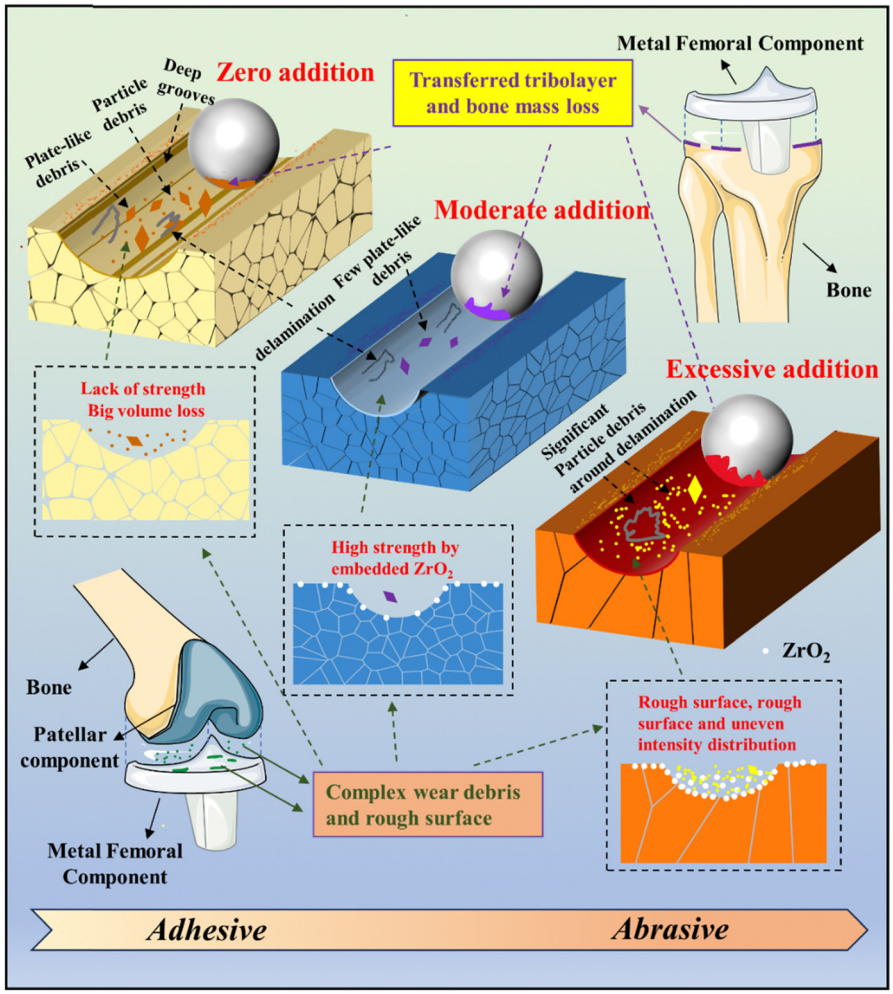

Fig. 15 Schematic and mechanism of tribological behavior in real implants.

with the high COF of Z0 led to strong adhesive wear. Adhesive wear can cause a transferred tribolayer as shown in Fig. 15.[57] This can further cause aseptic infections, blackening of tissues, and even negative impacts on other organs through fluid conduction.

When ZrO_2 content was optimal (*e.g.*, Z3 in this work), the increased yield strength from the ZrO_2 reinforcement made shear initiation at the implant surface more difficult. At this concentration, Zr, O solutes, and ZrO_2 particles collectively increased the matrix strength. As wear progressed, the appropriate content, size, and dispersion of ZrO_2 particles prevent significant debris agglomeration. EDS results indicated that *in vivo*, the bone or patellar component pressed most particles deeper into the material rather than displacing them. This pressing-in enhanced load-bearing and the Orowan effect, reducing the likelihood of significant fine debris formation in the abrasive medium.

However, the base wear performance of the composite decreased with ZrO_2 content >5 wt%, which was attributed to the specific mechanical strengthening mechanisms in these

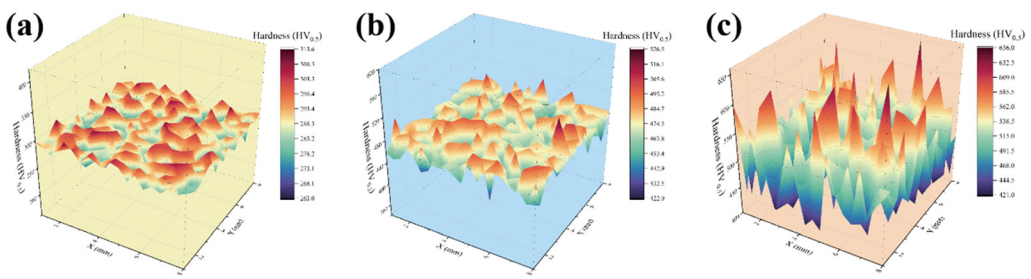

Fig. 16 Topological 3D hardness distribution of the three samples. (a) Z0; (b) Z3; (c) Z10.

samples. Fig. 16 shows that Z0 and Z3 had a relatively uniform hardness distribution in the wear test area. Z10, on the other hand, had an unstable hardness distribution due to its brittle nature and the presence of many macroscopic cracks. In other words, the integral value of $1/H(t)$ was not as small as expected all the time. The Hall–Petch strength of the Z10 matrix was actually undesirable due to the overly coarse prior β grains with multilayered microstructures and the piled-up Cu leading to an overly pathological dependence on excess ZrO_2 and coefficient of thermal expansion mismatch for strength. This large difference in strength also led to rough wear surfaces in the intermediate stages of wear, where particle debris was more likely to form than plate-like debris. These, together with partially dislodged ZrO_2, would cause significant abrasive wear, increasing pure wear loss. The volumetric loss of $\omega_{abrasive}$ due to abrasive wear can be modeled by the following equation:[56]

$$\omega_{abrasive} = K_{trans}\int_0^t \frac{2\overline{\tan\theta}}{\pi}\cdot\frac{F_n\cdot v}{H(t)}dt \quad (4)$$

where θ is the attack angle of the asperity. The aggregated ZrO_2 higher hardness led to a larger attack angle, which intensified abrasive wear. In addition, high elastic modulus values resulting from undesirable strengthening mechanisms were not only prone to the well-known stress shielding effect but also

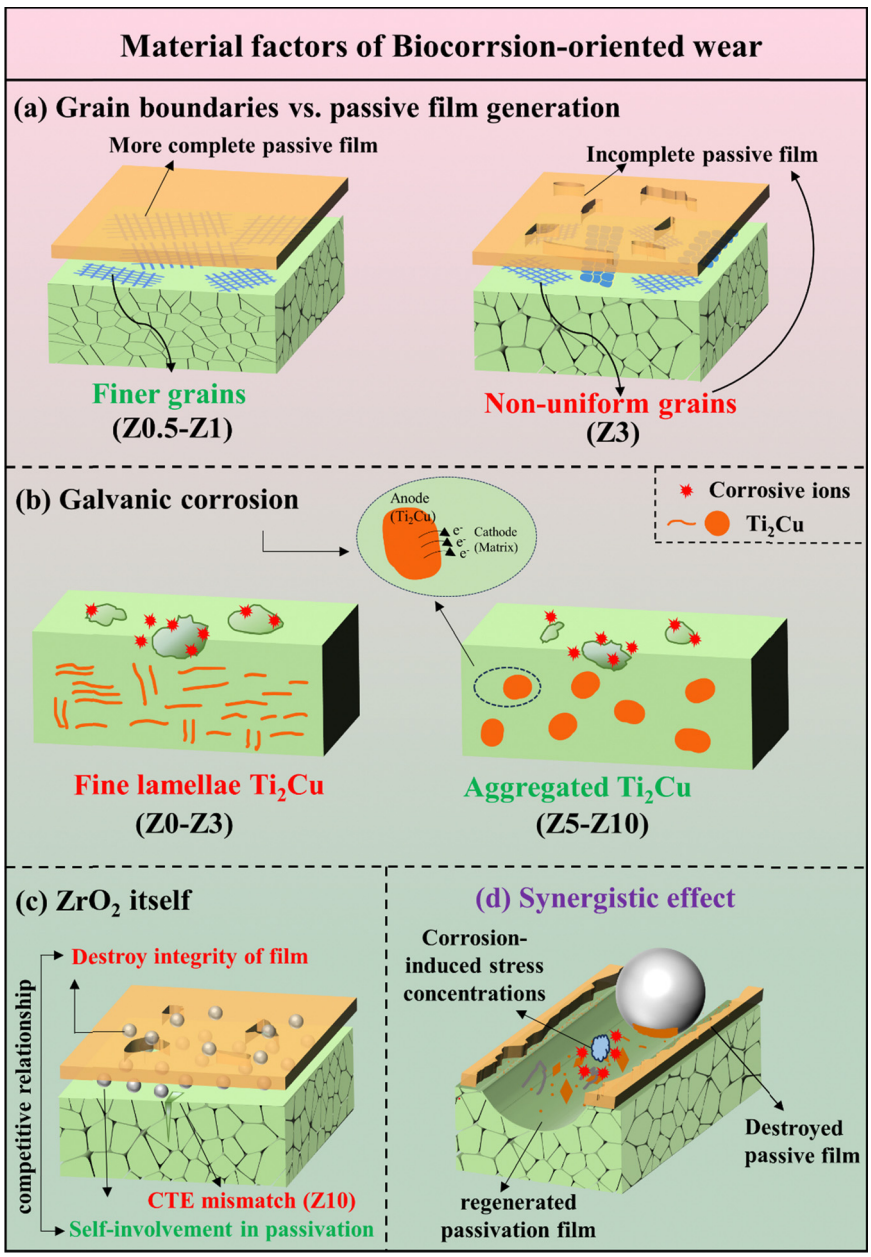

Fig. 17 Material aspects of the implantation process that affect biocorrosion-oriented wear. They are categorized as: (a) Grain boundaries & passive film generation; (b) glavanic corrosion; (c) ZrO_2 itself and (d) synergistic effect. Green lettering indicates the factors that enhance corrosion resistance. The red color indicates the factors that reduce corrosion resistance.

negatively impacted the wear performance. The Hertzian contact concept interprets the effect of elastic modulus on friction behavior.[10] The Hertzian contact diameter (HCD) and Hertzian contact pressure (HCP) of the friction pair (stainless steel ball) and composite in this work are defined by the following equations:[58]

$$\frac{1}{E_0} = \frac{1-\nu_1^2}{E_1} + \frac{1-\nu_2^2}{E_2} \quad (5)$$

$$\mathrm{HCD} = \sqrt[3]{\frac{6RP}{E_0}} \quad (6)$$

$$\mathrm{HCP} = \sqrt[3]{\frac{6PE_0^2}{\pi^2 \times R^2}} \quad (7)$$

where E_1 and E_2 represent the Young's modulus of the friction pair and the sample, and ν_1 and ν_2 represent their Poisson's ratios. P is the normal load and R is the radius of the friction pair. A high elastic modulus increases HCD and HCP, leading to an increased wear and a higher likelihood of bone defects.

Therefore, reasonable control of the ZrO_2 content optimized the mechanical strengthening mechanisms and thereby improved wear performance. The test results indicated that 3% was the optimum.

4.2.2 Biocorrosion-oriented wear mechanism. Despite the excellent corrosion resistance of titanium alloys to body fluids, Dong *et al.*[55] indicated that pure corrosion loss during wear in a corrosive media was only 0.1%. However, the wear mass loss due to corrosion accounted for about 14% of the total mass loss. The factors affecting the corrosion rate are equally, if not more, important than the corrosion rate values of the Ti–Cu alloy-based composites themselves, as they directly influence the extent of wear loss due to corrosion.[59]

Fig. 17 summarizes the factors that influence corrosion in this study: (a) Gollapudi's theory indicates that the size and uniformity of the microstructure significantly affect the integrity of the passivation film on titanium alloys.[60] In this regard, the Z3 sample, awkwardly positioned at the microstructural tipping point, possessed dual lamellar and equiaxed morphologies of α grains, resulting in the lowest R_f value; (b) the Ti_2Cu precipitate phase in LMDed Ti–Cu alloys is a major source of galvanic corrosion.[9] Therefore, the fineness of the Ti_2Cu precipitates determines the severity of galvanic corrosion, with denser Ti_2Cu (as in composites with no or minimal addition) being more susceptible to galvanic corrosion; (c) ZrO_2 itself also has a passivating effect, but excessive ZrO_2 can disrupt the integrity of the passive film, and the resultant cracks can increase the corrosion area.[31]

There are two reasons that lead to the exacerbation of wear by corrosion. First, during the corrosion and wear process, the passive film on the surface of the Ti matrix undergoes repeated removal and repassivation.[55] The strength of the regenerated passive film influences the subsequent material loss caused by wear. Second, the corrosion and dissolution of the wear tracks damage the original microstructure of the substrate surface, leading to localized stress concentration.[61]

The first reason is determined by the self-passivating ZrO_2 content, as well as the strength of the primary and regenerated passive films. However, this study found little correlation between R_f and R_p values, and the effect of ZrO_2 content on passivation is too complex to warrant further discussion. The second reason is primarily dictated by the intensity of galvanic corrosion. With equal Cu content, the fine distribution of Ti_2Cu leads to premature stress concentration due to corrosion on the substrate surface, exacerbating wear. This makes a low ZrO_2 content unfavorable, but excessive content results in cracks, significantly increasing stress concentration due to corrosion.

Overall, a moderate ZrO_2 content is beneficial for wear driven by biocorrosion. The corrosion results indicated 3–5 wt% was optimal. Considering the previous sections, 3% was the best for wear resistance.

4.3 Validation of bio-function and safe intake of elements

Ensuring the reliability of the composite's antibacterial function is a crucial part of the content screening and optimization in this work. Samples with two representative contents both exhibited good antibacterial performance against *E. coli*. Previous research indicated that the antibacterial mechanisms of the ZrO_2/Ti–Cu system primarily include:[29,49,62] (a) ROS

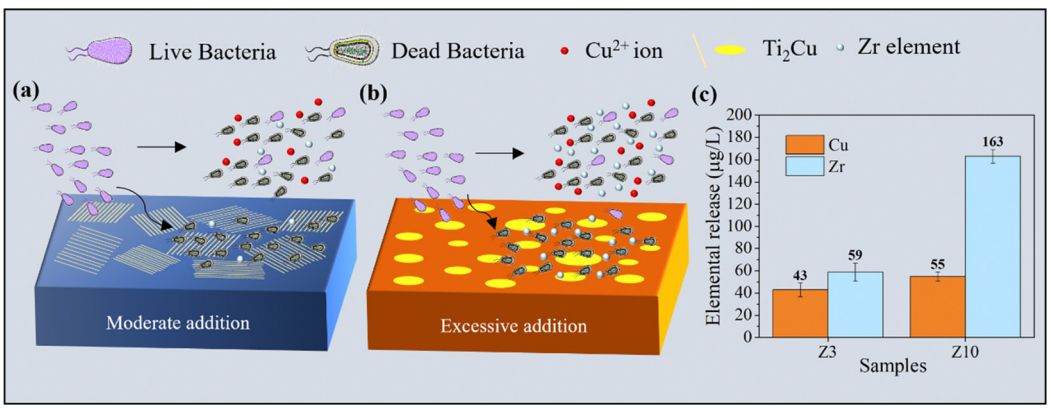

Fig. 18 (a) Schematic representation of the antibacterial mechanism of composites with moderate content; (b) schematic representation of the antibacterial mechanism of composites with excess content; (c) ICP-OES results of Cu and Zr release in the body fluid of Z3 and Z10.

production from Cu^{2+}, Ti_2Cu, and ZrO_2; (b) contact killing by the potential difference between Ti_2Cu, ZrO_2, and the Ti matrix; (c) $Zr^{(+)}$ induced cell membrane damage. The element distribution in the microstructure indicated that different ZrO_2 contents mainly affect the distribution of Ti_2Cu and the concentration of Zr, both of which are key antibacterial agents. Fig. 18(a) indicates that an appropriate ZrO_2 content results in a denser Ti_2Cu phase, which produced stronger contact killing.[63] However, Fig. 18(b) shows that an excessive ZrO_2 content also increases the concentration of another potential antibacterial agent, Zr. Therefore, sufficient Cu and Zr ensure the antibacterial effect.

However, for materials where the primary functionality is governed by heavy metal elements, it is essential to consider whether the concentrations of these elements exceed the safe human intake levels. Additionally, ROS generally cannot distinguish significantly between bacteria and cells, so its concentration must be carefully controlled.[64] Cu and ZrO_2 have dual effects on the proliferation of osteoblasts, acting as double-edged swords. A small amount of copper promotes osteoblast proliferation, whereas an excessive amount of copper can cause harmful effects.[65,66] Fortunately, *MC3T3-E1* test results indicate that the addition of Cu and ZrO_2 did not negatively impact the proliferation of osteoblasts compared to the control group and pure titanium. Fig. 18(c) shows that the ICP-OES test results provided further validation, as the concentrations of both elements were below their maximum safe concentrations for osteoblasts (10 mg L^{-1} for ZrO_2 and 227 μg L^{-1} for Cu).[6,29] This indicated that within the range of concentrations studied, ZrO_2 addition did not impair the antibacterial functionality of Cu and did not induce cytotoxicity.

5. Conclusions

This work investigated the effect of different ZrO_2 contents on the implantation-related mechanical properties, wear properties, body fluid corrosion resistance, antimicrobial properties, and biocompatibility of LMD Ti–3wt%Cu under optimal production parameters. The evaluation of these properties and mechanistic investigation identified the best as 3 wt% addition. The main conclusions were as follows:

(1) Z0–Z3 had relatively good macroformability. Z5 and Z10 had increasing macrocracks. Z0–Z3 mainly had a microstructure of prior equiaxed β grains. Z10 had prior β grains dominated by columnar grains. Z0–Z1 mainly had a fine basketweave grain pattern of α-Ti. Z5–Z10 mainly had coarse α colonies. Z3 had mostly fine basketweave grains with some equiaxed grains around prior β grain boundaries. The different thermal properties between zirconia and the alloy matrix determined the different processing and molding properties. Z0–Z3 met the requirements for mass production of implantable materials.

(2) The addition of ZrO_2 gradually transformed the samples from tough to brittle. Z3 had a YS 67% larger than Z0, a strain at fracture of 4.7% and a low Young's modulus (109 GPa). Z10 had a YS 167% larger than Z0, but only had a strain at fracture of 1.9% and a large Young's modulus (320 GPa). A good YS enhances the service life of bone implant materials, but too high Young's modulus leads to stress-shielding. Taken together, Z3 best meets the mechanical property requirements of the reinforced implantable material.

(3) The wear rate from smallest to largest was Z3 < Z5 < Z10 < Z1 < Z0. The wear mechanisms included adhesive wear, abrasive wear, oxidative wear, fatigue wear, *etc.*, with different contributions for each sample. Z3 had the smallest wear volume loss and the smoothest wear scar. The smaller wear rate can greatly delay the failure time of the bone implant material, while the smoother wear surface can make the surrounding tissues less susceptible to debris-related complications.

(4) ZrO_2 addition had little effect on the corrosion of Ti–3wt%Cu in the body fluid; nevertheless, Z3 and Z5 represented the best concentrations for corrosion resistance. The addition of moderate (Z3) or excessive (Z10) amounts of ZrO_2 to the Ti–3wt%Cu alloy did not have a significant adverse effect on their antimicrobial properties or their good biocompatibility. The antimicrobial rates of Z3 and Z10 were 99.4% and 95.7%, respectively. The RGR and the proliferation numbers of Z3 and Z10 were in accordance with requirements. The trace amounts of heavy metal ions did not adversely affect the adhesion and proliferation of osteoblasts.

Data availability

All data included in this study are available upon request by contact with the corresponding author.

Conflicts of interest

All authors agreed to this submission and declare no conflicts of interest.

Acknowledgements

Financially supported by the Natural Science Foundation of Shandong Province (no. ZR2023ME181), the National Natural Science Foundation of China (no. 52305313) and the Natural Science Foundation of Hunan Province (no. 2023JJ40553).

References

1 M. Geetha, A. K. Singh, R. Asokamani and A. K. Gogia, Ti based biomaterials, the ultimate choice for orthopaedic implants – A review, *Prog. Mater. Sci.*, 2009, **54**, 397–425.
2 M.-M. Germaini, S. Belhabib, S. Guessasma, R. Deterre, P. Corre and P. Weiss, Additive manufacturing of biomaterials for bone tissue engineering – A critical review of the state of the art and new concepts, *Prog. Mater. Sci.*, 2022, **130**, 100963.
3 M. Bahraminasab, B. B. Sahari, K. L. Edwards, F. Farahmand, M. Arumugam and T. S. Hong, Aseptic loosening of femoral components – A review of current

and future trends in materials used, *Mater. Des.*, 2012, **42**, 459–470.
4 C. R. Gerhart, S. P. Boddu, J. M. Haglin and J. S. Bingham, Revision arthroplasty among medicare patients in the united states – arthroplasty surgeons are doing more for less, *J. Arthroplasty*, 2024, **39**, S81–S87.
5 M. J. DeFrance and G. R. Scuderi, Are 20% of patients actually dissatisfied following Total Knee Arthroplasty? A systematic review of the literature, *J. Arthroplasty*, 2023, **38**, 594–599.
6 W. Zhang, M. Zhao, Z. Wang, L. Tan, Y. Qi, D. Yin, K. Yang and A. Atrens, Enhanced initial biodegradation resistance of the biomedical Mg–Cu alloy by surface nanomodification, *J. Magnesium Alloys*, 2022, **11**, S2213956722000093.
7 Y. Guo, M.-C. Zhao, B. Xie, Y.-C. Zhao, D. Yin, C. Gao, C. Shuai and A. Atrens, *In vitro* corrosion resistance and antibacterial performance of novel fe–xcu biomedical alloys prepared by selective laser melting, *Adv. Eng. Mater.*, 2021, **23**, 2001000.
8 B. Xie, M. Zhao, R. Xu, Y. Zhao, D. Yin, C. Gao and A. Atrens, Biodegradation, antibacterial performance, and cytocompatibility of a novel ZK30-Cu-Mn biomedical alloy produced by selective laser melting, *Int. J. Bioprint.*, 2020, **7**, 300.
9 H. Ji, M.-C. Zhao, B. Xie, Y.-C. Zhao, D. Yin, C. Gao, C. Shuai and A. Atrens, Corrosion and antibacterial performance of novel selective-laser-melted (SLMed) Ti-xCu biomedical alloys, *J. Alloys Compd.*, 2021, **864**, 158415.
10 A. Afrouzian and A. Bandyopadhyay, 3D printed silicon nitride, alumina, and hydroxyapatite ceramic reinforced Ti6Al4V composites – Tailored microstructures to enhance bio-tribo-corrosion and antibacterial properties, *J. Mech. Behav. Biomed. Mater.*, 2023, **144**, 105973.
11 K. Moghadasi, M. S. Mohd Isa, M. A. Ariffin, M. Z. Mohd jamil, S. Raja, B. Wu, M. Yamani, M. R. Bin Muhamad, F. Yusof, M. F. Jamaludin, M. S. bin Ab Karim, B. binti Abdul Razak and N. bin Yusoff, A review on biomedical implant materials and the effect of friction stir based techniques on their mechanical and tribological properties, *J. Mater. Res. Technol.*, 2022, **17**, 1054–1121.
12 X. Li, Y. Zhao, D. F. Yin, Y. Cai, D. S. Xiao, M. C. Zhao, C. E. Wen and A. Atrens, Microwave-sintered nano-SiC reinforced 8SiC/Ti–3Cu composite: fabrication, wear resistance, antibacterial function, and biocompatibility, Advanced Healthcare, *Materials*, 2025, **14**, 2403626.
13 S. Moniri Javadhesari, S. Alipour and M. R. Akbarpour, Microstructural characterization and enhanced hardness, wear and antibacterial properties of a powder metallurgy SiC/Ti–Cu nanocomposite as a potential material for biomedical applications, *Ceram. Int.*, 2019, **45**, 10603–10611.
14 D. Xu, T. Wang, Z. Lu, Y. Wang, B. Sun, S. Wang, Q. Fu, Z. Bi and S. Geng, Ti-6Al-4V-5Cu synthesized for antibacterial effect *in vitro* and *in vivo via* contact sterilization, *J. Mater. Sci. Technol.*, 2021, **90**, 133–142.
15 Y. Xie, Y. Peng, G. Fu, J. Jin, S. Wang, M. Li, Q. Zheng, F.-J. Lyu, Z. Deng and Y. Ma, Nano wear particles and the periprosthetic microenvironment in aseptic loosening induced osteolysis following joint arthroplasty, *Front. Cell. Infect. Microbiol.*, 2023, **13**, 1275086.
16 N. A. Hodges, E. M. Sussman and J. P. Stegemann, Aseptic and septic prosthetic joint loosening: Impact of biomaterial wear on immune cell function, inflammation, and infection, *Biomaterials*, 2021, **278**, 121127.
17 Z. Liu, M. Zhao, D. Yin, Y. Zhao and A. Atrens, Biofunctional niobium-based metallic biomaterials: Exploring their physicomechanical properties, biological significance, and implant applications, *Acta Biomater.*, 2025, **192**, 1–27.
18 L. Huang, Q. An, L. Geng, S. Wang, S. Jiang, X. Cui, R. Zhang, F. Sun, Y. Jiao, X. Chen and C. Wang, Multiscale Architecture and Superior High-Temperature Performance of Discontinuously Reinforced Titanium Matrix Composites, *Adv. Mater.*, 2021, **33**, 2000688.
19 C. Han, R. Babicheva, J. D. Q. Chua, U. Ramamurty, S. B. Tor, C.-N. Sun and K. Zhou, Microstructure and mechanical properties of (TiB + TiC)/Ti composites fabricated *in situ via* selective laser melting of Ti and B4C powders, *Addit. Manuf.*, 2020, **36**, 101466.
20 J. L. Li, M. C. Zhao, Y. C. Zhao, D. F. Yin and A. Atrens, Customization and prospects of friction stirprocessing for improving the biomedicalproperties of metallic implants fororthopedic applications, *J. Mater. Res. Technol.*, 2025, **34**, 2133–2149.
21 D. Gu, X. Shi, R. Poprawe, D. L. Bourell, R. Setchi and J. Zhu, Material-structure-performance integrated laser-metal additive manufacturing, *Science*, 2021, **372**, eabg1487.
22 E. Fereiduni, A. Ghasemi and M. Elbestawi, Unique opportunities for microstructure engineering via trace B4C addition to Ti-6Al-4V through laser powder bed fusion process: As-built and heat-treated scenarios, *Addit. Manuf.*, 2022, **50**, 102557.
23 S. M. Thompson, L. Bian, N. Shamsaei and A. Yadollahi, An overview of Direct Laser Deposition for additive manufacturing; Part I: Transport phenomena, modeling and diagnostics, *Addit. Manuf.*, 2015, **8**, 36–62.
24 L. Wang, Z. Song, X. Zhang, J.-S. Park, J. Almer, G. Zhu, Y. Chen, Q. Li, X. Zeng and Y. Li, Developing ductile and isotropic Ti alloy with tailored composition for laser powder bed fusion, *Addit. Manuf.*, 2022, **52**, 102656.
25 N. Singh, P. Hameed, R. Ummethala, G. Manivasagam, K. G. Prashanth and J. Eckert, Selective laser manufacturing of Ti-based alloys and composites: impact of process parameters, application trends, and future prospects, *Mater. Today Adv.*, 2020, **8**, 100097.
26 J. Song, Y. Liu, Z. Liao, S. Wang, R. Tyagi and W. Liu, Wear studies on ZrO_2-filled PEEK as coating bearing materials for artificial cervical discs of Ti6Al4V, *Mater. Sci. Eng., C*, 2016, **69**, 985–994.
27 M. S. Abd-Elwahed, A. F. Ibrahim and M. M. Reda, Effects of ZrO_2 nanoparticle content on microstructure and wear behavior of titanium matrix composite, *J. Mater. Res. Technol.*, 2020, **9**, 8528–8534.
28 Z. Ur Rehman and D. Choi, Investigation of ZrO_2 nanoparticles concentration and processing time effect on the

localized PEO coatings formed on AZ91 alloy, *J. Magnesium Alloys*, 2019, **7**, 555–565.

29 N. Tabassum, D. Kumar, D. Verma, R. A. Bohara and M. P. Singh, Zirconium oxide (ZrO_2) nanoparticles from antibacterial activity to cytotoxicity: A next-generation of multifunctional nanoparticles, *Mater. Today Commun.*, 2021, **26**, 102156.

30 H. Han, S. Li, M. Xu, Y. Zhong, W. Fan, J. Xu, T. Zhou, J. Ji, J. Ye and K. Yao, Polymer- and lipid-based nanocarriers for ocular drug delivery: Current status and future perspectives, *Adv. Drug Delivery Rev.*, 2023, **196**, 114770.

31 X. Zhou, M. Zhang, D. Xu, S. Geng, Q. Wang and F. Wang, Microstructural evolution, corrosion behavior and cytotoxicity of Ti-6Al-4V/ZrO_2 composite fabricated by directed energy deposition for implant biomaterial, *J. Alloys Compd.*, 2022, **892**, 161820.

32 J. Li, L. Shen, Z. Liu, H. Liang, Y. Li and X. Han, Microstructure, microhardness, and wear performance of zirconia reinforced pure titanium composites prepared by selective laser melting, *Mater. Res. Express*, 2018, **6**, 036520.

33 Z. Ouyang, H. Jin, Q. Cheng, W. Chen, Y. Wei and J. Chen, Macro–micro residual stress prediction and hot crack formation mechanism during laser melt injection processing of ZrO_2 particles into Ti6Al4V substrate, *Int. J. Adv. Manuf. Technol.*, 2022, **121**, 3637–3651.

34 M. Fang, Y. Han, Z. Shi, G. Huang, J. Song and W. Lu, Embedding boron into Ti powder for direct laser deposited titanium matrix composite: Microstructure evolution and the role of nano-TiB network structure, *Composites, Part B*, 2021, **211**, 108683.

35 H. Attar, S. Ehtemam-Haghighi, D. Kent and M. S. Dargusch, Recent developments and opportunities in additive manufacturing of titanium-based matrix composites: A review, *Int. J. Mach. Tools Manuf.*, 2018, **133**, 85–102.

36 J. D. Avila, K. Stenberg, S. Bose and A. Bandyopadhyay, Hydroxyapatite reinforced Ti6Al4V composites for load-bearing implants, *Acta Biomater.*, 2021, **123**, 379–392.

37 X. Zhang, D. Li, Y. Zheng, P. Shojaei, M. Trabia, B. O'Toole, D. Lin, L. Mushongera and Y. Liao, In-situ synthesis of Ti5Si3-reinforced titanium matrix nanocomposite by selective laser melting: Quasi-continuous reinforcement network and enhanced mechanical performance, *J. Mater. Process. Technol.*, 2022, **309**, 117752.

38 C. D. Gao, M. Yao, C. J. Shuai, S. P. Peng and Y. W. Deng, Nano-SiC reinforced Zn biocomposites prepared via laser melting: Microstructure, mechanical properties and biodegradability, *J. Mater. Sci. Technol.*, 2019, **35**, 2608–2617.

39 M. Wu, M. Zhao, Y. Cai, J. Yao, P. Wang and A. Atrens, Recent advances in bio-functional Ta-based bone materials: materials design and bioactivity, *Extreme*, 2024, **6**, 062010.

40 Y. Zhao, Y. Tang, M. Zhao, L. Liu, C. Gao, C. Shuai, R. Zeng, A. Atrens and Y. Lin, Graphene Oxide Reinforced Iron Matrix Composite With Enhanced Biodegradation Rate Prepared by Selective Laser Melting, *Adv. Eng. Mater.*, 2019, **21**, 1900314.

41 M. Zhao, Y. Zhao, D. Yin, S. Wang, Y. Shangguan, C. Liu, L. Tan, C. Shuai, K. Yang and A. Atrens, Biodegradation behavior of coated as-extruded Mg–Sr alloy in simulated body fluid, *Acta Metall. Sin.*, 2019, **32**, 1195–1206.

42 J. Jin, S. Zhou, W. Zhang, K. Li, Y. Liu, D. Chen and L.-C. Zhang, Effect of ceramic types on the microstructure and corrosion behavior of titanium matrix composites produced by selective laser melting, *J. Alloys Compd.*, 2022, **918**, 165704.

43 Y. Zou, C. Tan, Z. Qiu, W. Ma, M. Kuang and D. Zeng, Additively manufactured SiC-reinforced stainless steel with excellent strength and wear resistance, *Addit. Manuf.*, 2021, **41**, 101971.

44 D. Zhang, D. Qiu, M. A. Gibson, Y. Zheng, H. L. Fraser, D. H. StJohn and M. A. Easton, Additive manufacturing of ultrafine-grained high-strength titanium alloys, *Nature*, 2019, **576**, 91–95.

45 H. Wang, C. Yu, Z. Yu, Y. Huang, X. Zhang, L. Mei, J. Chen, Y. Wang, H. Lu and J. Xu, Revealing the evolution of microstructure and mechanical properties with energy density to achieve high-strength Ti-6wt%Cu alloy by laser metal deposition, *Mater. Sci. Eng., A*, 2023, **885**, 145599.

46 J. Feng, Z. Shi, Y. Zhao, J. Wang, X. Yang and M. Zhao, Surface performance of nano-CrN/TiN multi-layered coating on the surface of Ti alloy, *Materials*, 2023, **16**, 7707.

47 Z. Song, Y. Cai, X. Li, Y. Zhao, D. Yin, A. Atrens and M. Zhao, Fresh insights into structure–function-integrated self-antibacterial Cu-containing Al alloys: giving Al alloys a new function, *Mater. Horiz.*, 2025, **12**, 814–832.

48 R. Arrabal, B. Mingo, A. Pardo, M. Mohedano, E. Matykina and I. Rodríguez, Pitting corrosion of rheocast A356 aluminium alloy in 3.5 wt% NaCl solution, *Corros. Sci.*, 2013, **73**, 342–355.

49 J. Li, D. Zhang, X. Chen, D. Xu, D. Qiu, F. Wang and M. Easton, Laser directed energy deposited, ultrafine-grained functional titanium-copper alloys tailored for marine environments: Antibacterial and anti-microbial corrosion studies, *J. Mater. Sci. Technol.*, 2023, **166**, 21–33.

50 T. DebRoy, H. L. Wei, J. S. Zuback, T. Mukherjee, J. W. Elmer, J. O. Milewski, A. M. Beese, A. Wilson-Heid, A. De and W. Zhang, Additive manufacturing of metallic components – Process, structure and properties, *Prog. Mater. Sci.*, 2018, **92**, 112–224.

51 E. Fereiduni, A. Ghasemi and M. Elbestawi, Microstructural characterization and mechanical properties of nano-scale/submicron TiB-reinforced titanium matrix composites fabricated by laser powder bed fusion, *J. Alloys Compd.*, 2022, **896**, 163054.

52 X. Wang, L.-J. Zhang, J. Ning, S. Li, L.-L. Zhang and J. Long, Hierarchical grain refinement during the laser additive manufacturing of Ti-6Al-4V alloys by the addition of micron-sized refractory particles, *Addit. Manuf.*, 2021, **45**, 102045.

53 S. Zhang, J. Yao, P. Wang, H. Wang and J. Zhang, Formation of the Primary Second Phases and their Influence on the Mechanical Properties of an as-Cast Al–Li–Mg Alloy with Multi-Microalloying (Sc, Zr, Er and Ti), *Int. J. Metalcast.*, 2024, **18**, 608–619.

54 S. W. Watson, F. J. Friedersdorf, B. W. Madsen and S. D. Cramer, Methods of measuring wear-corrosion synergism, *Wear*, 1995, **181–183**, 476–484.

55 K. Dong, Y. Song, G. Bian, Y. Cai and E.-H. Han, Tribocorrosion behavior of TC18 titanium alloy: A discussion about the

interaction between galvanic corrosion and wear, *Tribol. Int.*, 2024, **192**, 109292.
56 W. Xu, W. Li and Y. Wang, Experimental and theoretical analysis of wear mechanism in hot-forging die and optimal design of die geometry, *Wear*, 2014, **318**, 78–88.
57 P. Jiang, Y. Zhang, R. Hu, B. Shi, L. Zhang, Q. Huang, Y. Yang, P. Tang and C. Lin, Advanced surface engineering of titanium materials for biomedical applications: From static modification to dynamic responsive regulation, *Bioact. Mater.*, 2023, **27**, 15–57.
58 A. Pandey, V. K. Nigam and K. Balani, Multi-length scale tribology of hydroxyapatite reinforced with ceria and silver, *Wear*, 2018, **404–405**, 12–21.
59 Z. Zheng, M. C. Zhao, L. Tan, Y. C. Zhao, B. Xie, D. Yin, K. Yang and A. Atrens, Corrosion behavior of a self-sealing coating containing CeO2 particles on pure Mg produced by micro-arc oxidation, *Surf. Coat. Technol.*, 2020, **386**, 125456.
60 S. Gollapudi, Grain size distribution effects on the corrosion behaviour of materials, *Corros. Sci.*, 2012, **62**, 90–94.
61 J. Su, J. Teng, Z. Xu and Y. Li, Corrosion-wear behavior of a biocompatible magnesium matrix composite in simulated body fluid, *Friction*, 2022, **10**, 31–43.
62 M. Vincent, R. e Duval, P. Hartemann and M. Engels-Deutsch, Contact killing and antimicrobial properties of copper, *J. Appl. Microbiol.*, 2018, **124**, 1032–1046.
63 P. Mahmoudi, M. R. Akbarpour, H. B. Lakeh, F. Jing, M. R. Hadidi and B. Akhavan, Antibacterial Ti–Cu implants: A critical review on mechanisms of action, *Mater. Today Bio*, 2022, **17**, 100447.
64 J. Li, J. Ma, H. Sun, M. Yu, H. Wang, Q. Meng, Z. Li, D. Liu, J. Bai, G. Liu, X. Xing, F. Han and B. Li, Transformation of arginine into zero-dimensional nanomaterial endows the material with antibacterial and osteoinductive activity, *Sci. Adv.*, 2023, **9**, eadf8645.
65 X. Yan, P. Wan, L. Tan, M. Zhao, C. Shuai and K. Yang, Influence of hybrid extrusion and solution treatment on the microstructure and degradation behavior of Mg–0.1Cu alloy, *Mater. Sci. Eng., B*, 2018, **229**, 105–117.
66 P. Tsvetkov, S. Coy, B. Petrova, M. Dreishpoon, A. Verma, M. Abdusamad, J. Rossen, L. Joesch-Cohen, R. Humeidi, R. D. Spangler, J. K. Eaton, E. Frenkel, M. Kocak, S. M. Corsello, S. Lutsenko, N. Kanarek, S. Santagata and T. R. Golub, Copper induces cell death by targeting lipoylated TCA cycle proteins, *Science*, 2022, **375**, 1254–1261.